

A study of dead water resistance

Reynolds Averaged Navier Stokes simulations of a barge moving in stratified waters

Peter Even Killingstad

Master's Thesis, Spring 2018



This master's thesis is submitted under the master's programme *Computational Science and Engineering*, with programme option *Mechanics*, at the Department of Mathematics, University of Oslo. The scope of the thesis is 30 credits.

The front page depicts a section of the root system of the exceptional Lie group E_8 , projected into the plane. Lie groups were invented by the Norwegian mathematician Sophus Lie (1842–1899) to express symmetries in differential equations and today they play a central role in various parts of mathematics.

Abstract

Computational fluid dynamics, with the software OpenFOAM, has been used to investigate the dead water phenomenon. Investigation was done by simulating a barge moving in stratified waters. Comparison of the turbulence models $k - \epsilon$ and $k - \omega$ SST has been conducted, resulting in a better performance in estimating drag by the $k - \omega$ SST model. Simulations of the barge moving in stratified fluid is shown to generate internal gravity waves below and in the wake of the barge. The internal gravity waves cause the barge to experience an increase in drag for subcritical densimetric Froude numbers (Fr_h). Maximum drag is shown to appear in regions of $0.6 \leq Fr_h \leq 0.7$. Internal gravity waves restrict the passage area causing an acceleration of the flow downstream of the barge, resulting in thinning of boundary layer and in drop of pressure.

Acknowledgements

First of all i would like to thank my supervisor associate professor Mikael Mortensen for insightful conversations and guidance.

I would also like to thank fellow students who have made these two years a bit easier to carry out. I would especially like to thank Karl Jacobsen for many fun, profound and insightful conversations of all kinds of subjects, both academic and social.

Finally, I would like to thank my mother and Knut Smidsrød for trying to correct my rather weak grammatical performance of the English language.

Contents

1	Introduction	1
2	Theory: Governing equations, Turbulence, and Numerical methods.	4
2.1	Governing equations	4
2.2	Turbulence	6
2.2.1	Physical concepts of turbulence	6
2.2.2	Boundary layer	7
2.2.3	Computer modelling of turbulence	8
2.3	Volume of fluid	12
2.4	Numerical discretization	13
3	OpenFOAM	15
3.1	Introduction to OpenFoam	15
3.2	TwoLiquidMixingFoam	17
3.3	Turbulence models	17
3.4	Numerical schemes	18
3.5	Solution algorithms	19
4	Simulation Design	20
4.1	Simulation geometry	20
4.2	Simulation set-up	21
4.3	Boundary and Initial conditions	22
4.3.1	U	24
4.3.2	alpha.saltWater	25
4.3.3	p_rgh	25
4.3.4	Turbulence properties k, nut, omega and epsilon	26
4.4	Mesh and mesh convergence	27
4.4.1	Meshing procedure	27
4.4.2	Convergence tests	29
5	Results	32
5.1	Comparison of turbulence models	32
5.2	Drag	33
5.2.1	Non-stratified fluid	33
5.2.2	Stratified fluids	34
5.3	Internal wave and its effect	36
5.3.1	Internal waves and effect on velocity	37

6	Conclusions and further recommendations	40
6.1	Conclusions	40
6.2	Further recommendations	41

Chapter 1

Introduction

Dead water is the phenomenon where internal gravity waves are causing boats or vessels moving along the surface of a stratified fluid, to experience increased drag force. A stratified fluid can be observed in the ocean where layers have different salinity, or temperature jumps, causing a difference in density. Rapidly melting glaciers can produce a layer of fresh water on top of denser ocean salt water, or a layer of warmer ocean currents can be lying on top of colder currents. The internal gravity waves occur where the maximum vertical density gradient exist, called the pycnocline.

The Norwegian scientist and explorer Fridtjof Nansen was the first to describe the phenomenon [1]. During the FRAM expedition while passing north of Sibira, his boat FRAM experienced a reduction in speed to about a fifth, even though the engine was working on full power. As the speed was reduced, F. Nansen observed internal waves across the wake, arising sometimes as far as almost midships. Ekman later conducted the first experimental study on the phenomenon[2], by using a towing tank with stratified water conditions. The study concluded that the model experienced an increase in drag force due to the internal waves.

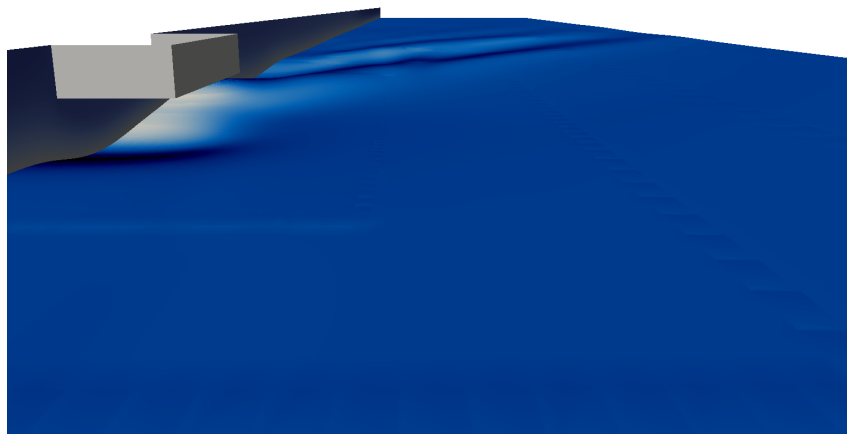


Figure 1.1: Internal wave below a barge

Visualization of an internal wave below and in the wake of a barge made by simulating with Computational fluid dynamics. The internal waves occur at the pycnocline located at 0.2 m below the surface.

This project is mainly motivated by the recently published work of J. Grue [5], Gou et al. [3] and Esmailpour et al. [4].

J. Grue investigated the dead water resistance on the Polar ship FRAM by using two methods. The first is empirical, using F. Nansens own observations, and the other is a strongly non linear interfacial method in three dimensions.

Gou et al. investigated drag force on a barge in two layer fluid. The investigation was done by conducting three dimensional experiments in a towing tank.

Esmailpour et al. studied dead water resistance on a vessel by simulating the phenomenon using computational fluid dynamics.

The Navier-Stokes equation is the fundamental equation describing viscous fluid flow, including the dead water phenomenon. In this project, the dead water phenomenon is studied by using computational fluid dynamics. In order to fully resolve the 3-dimensional Navier-Stokes equation, computer simulation and discretization is needed as no explicit solution exists. Simulations of experiments on a barge moving in stratified water is done by using the free open source software OpenFOAM.

The main focus of the project is to study the drag force and the increase in drag due to stratified water. Non-stratified and stratified fluid simulations are conducted for qualitative understanding and comparison. Three different pycnocline depths are simulated for the stratified fluid experiments. Simulations are done with different speeds in order to obtain densimetric Froude numbers in regions $0.35 \leq Fr_h \leq 1.35$.

Increase in drag is presented for each pycnocline depth. Peak drag is shown to occur within a range of densimetric Froude number of $0.6 < Fr_h < 0.7$. The position of the internal gravity wave and its location below the barge is shown to have significant effect on the drag. Depending on the location of the internal gravity waves, velocity profiles below the stern of the barge are shown to be significantly effected

As the barge is moving through the stratified water, the flow is turbulent. To fully obtain details of the rapidly fluctuating flow is impossible, as it requires a huge amount of computational power. Various techniques of modelling turbulent flow are presented. This project is using Reynolds averaged Navier-Stokes (RANS) equations, a method focusing on the mean fluid flow. Two RANS turbulence models are presented, tested and compared to find the most suitable model for simulating dead water.

Stratified fluid simulations deal with fresh and salt water with different densities. OpenFOAM has several multi phase solvers implemented. This project is using the solver *twoLiquidMixingFoam* which solves the multi phase problem using the volume of fluid-method, and is applicable for two miscible fluids.

OpenFOAM is using the finite volume method, a numerical technique to discretize the equations. Brief motivation for applying the method is presented, along with a differential scheme. A computational domain has been made that consists of a mesh grid in which the discretized equations can be solved. The computational domain needs to be well defined at the boundaries in order to get meaningful results. Initial and boundary conditions are defined for all the variables in the equations.

Quality of the mesh is essential in order to get reliable results. Convergence tests of three systematically refined grids are conducted to make sure that the mesh used in the simulations are stable, and at the same time is computational efficient.

In the following chapters, theory, introduction to OpenFOAM, simulation design, results and finally a conclusion is presented.

The first chapter contains introduction to the governing equations of the thesis. It further gives a brief description of physical concepts of turbulence, boundary layer theory and computer modelling of turbulence. The theory behind the volume of fluid-method is presented, and finally an outline of the finite volume-method used to discretize the equations is presented.

The following chapter introduces the open software OpenFOAM, and its structure used in the solving procedure.

The simulation design chapter describes the numerical experiment, with domain geometry and physical setup. It further presents Initial and boundary conditions before mesh quality and convergence tests are presented.

The results are shown and discussed. A conclusion is reached and further recommendations are presented.

Chapter 2

Theory: Governing equations, Turbulence, and Numerical methods.

2.1 Governing equations

The study of viscous flow reaches back to ancient times. Humans figured out, with clever intuition, trial and error, the importance of viscous friction. Long before any real theoretical understanding of fluid flow, streamlined weapons and boats have been made to overcome the effects of viscosity. In more recent years the understanding has taken huge leaps. Today we have tools to master viscous flow with the help from theory. The fundamental equation describing viscous flow is called Navier-Stokes equation[7]. With the following assumptions: incompressible, newtonian fluids. Density and viscosity may be different, but for one fluid it is constant. This gives the following equations:

$$\nabla \cdot \mathbf{u} = 0 \quad (2.1)$$

$$\frac{\partial \rho \mathbf{u}}{\partial t} + \nabla \cdot (\rho \mathbf{u} \mathbf{u}) = \nabla p + \mu \nabla^2 \mathbf{u} + \rho \mathbf{g} + \mathbf{f}_{st} \quad (2.2)$$

where (2.1) is the conservation of mass and (2.2) is the conservation of momentum. \mathbf{u} is the velocity, p is the pressure, density is given by $\rho(\mathbf{x}, t)$, the dynamic viscosity is given by μ , \mathbf{g} and \mathbf{f}_{st} is the gravity and surface tension respectively. There are four independent variables, the spatial x, y and z coordinates, and the time t .

The equations are a set of coupled differential equations. In practice, these equations are too difficult to solve analytically, but solutions for some simple geometries and boundary conditions can be found. More complex cases, as almost all flows of engineering significance, needs to be approximated with numerical techniques. Computational fluid dynamics has become the most viable tool to represent the complex Navier-Stokes equations. Some CFD models will be briefly introduced later in this chapter.

Using Navier-Stokes (2.1 and 2.2), the goal would be to investigate the forces in most industrial and academic applications. Finding solutions to the equations, either analytical or approximate, makes it possible to calculate the force vector by using:

$$\mathbf{F} = \int_{surface} \left(\nu (\nabla \mathbf{u} + (\nabla \mathbf{u})^T) - p \mathbf{I} \right) \cdot \mathbf{n} ds. \quad (2.3)$$

\mathbf{n} is the unit vector normal to the surface, \mathbf{I} is the unit matrix and ν is the kinematic viscosity.

Having obtained the force vector, it is common to quantify the drag force or resistance by introducing the drag coefficient, a dimensionless quantity given by

$$C_d = \frac{F_d}{\frac{1}{2}\rho S u^2}. \quad (2.4)$$

Here F_d is the drag force, ρ is density, u is the freestream velocity and S is the surface area.

Viscous flows can be divided into several regimes, and the primary controlling parameter is the dimensionless Reynolds number[7].

$$Re = \frac{u_0 l_0}{\nu} \quad (2.5)$$

where u is a velocity scale, l_0 is a characteristic geometric size and ν is the kinematic viscosity. Re represents the ratio of inertial forces to viscous forces within a fluid flow. Fluid properties can cause dramatic changes to the flow patterns. It is usual to divide flows into three distinct regimes.

- Low Re flow:
Viscous forces dominate and the flow is smooth or in a laminar regime.
- Intermediate Re flow:
Flow is in a transitional region where it is partly fluctuating and partly in a laminar regime.
- High Re flow:
Inertial forces dominate and the flow is fluctuating or in a turbulent regime.

Objects advancing through fluids such as water generate free surface waves. At the same time, if an object is advancing through stratified fluids, it generates internal waves. While free surface waves depend on the Froude number:

$$Fr = \frac{U_0}{\sqrt{gL_0}}, \quad (2.6)$$

internal waves depend on the densimetric Froude number:

$$Fr_h = \frac{U_0}{c^*}. \quad (2.7)$$

U_0 is the ship speed, g is gravity and L_0 is the ship length at water level. c^* represents the celerity of the longest internal waves. For an infinitely deep stratified fluid, c^* is given as:

$$c^* = \sqrt{gh \frac{\Delta\rho}{\rho_0}} \quad (2.8)$$

where h is the distance from the free surface to the pycnocline, $\Delta\rho$ is the difference between the density of the stratified fluid.

2.2 Turbulence

2.2.1 Physical concepts of turbulence

Turbulence is the phenomenon where a fluid flow appears to be chaotic and random. Unlike laminar flow, where the fluid flows in an orderly fashion, turbulent flow is rapidly fluctuating in all spatial dimensions. Structures of the flow is varying from large scales comparable to the dimensions of the physical boundaries to small scales.

The main characteristics of turbulence is the transfer of energy from larger spatial scales into smaller, happening in a three dimensional space and time.

To discuss the main characteristics of turbulence, a useful concept is that of an "eddy". An eddy can be thought of as typical turbulence pattern of small- and large- scales all co-existing in the same fluid. The eddies consist of vortexes intertwined in a chaotic manner, being stretched by the mean flow and pulled in random directions by one another. This mechanism ultimately leads to braking of the eddies into smaller ones, leading to an "energy cascade"[12].

The kinetic energy of the mean flow is extracted by the largest scale eddies. Energy from the largest eddies is further extracted to smaller scales, and the kinetic energy is finally dissipated into thermal energy by the small scale eddies [12].

The turbulent kinetic energy is defined by the units $\sim [m^2/s^2] \sim u_0^2$. As turbulence is dissipative, the dissipation rate has the units $[m^2/s^3]$. The dissipation rate of kinetic energy scales as $\epsilon \propto u_0^3/l_0$ [10], where u_0 and l_0 is the characteristic velocity and length of the flow.

The dissipation rate of kinetic energy is one of the most important results of turbulence theory, and is referred to as the Kolmogorov relation [10]. A turbulent eddy with kinetic energy u_0^2 either loses its energy or breaks up into smaller eddies in one time scale or period $T \sim l_0/u_0$.

As Reynolds number is very large for turbulent flow, i.e $\frac{u_0 l_0}{\nu} \gg 1$, the large scale eddies are independent of the viscosity. To see how viscosity is effecting the turbulent flow, "Kolmogorov micro-scales" can be constructed. Using kinematic viscosity ν and the dissipation rate ϵ , small scale for velocity, length and time can be written out as:

$$\eta = \left(\frac{\nu^3}{\epsilon}\right)^{1/4}, \quad (2.9)$$

$$v = (\nu\epsilon)^{1/4}, \quad (2.10)$$

$$\tau = \left(\frac{\nu}{\epsilon}\right)^{1/2}, \quad (2.11)$$

where η is the micro length-scale, v is the velocity and τ is the time scale. Reynolds number in the "micro-scale" is given by $\frac{v\eta}{\nu} = 1$, hence the viscosity is of big importance at these scales. We have that the "micro-scale" eddies is dominated by friction, and small-scale turbulence is almost independent of large scale turbulence for large enough Reynolds number.

2.2.2 Boundary layer

Using Reynolds number (2.5) it is easily shown that, for a thin shear layer flow over a flat plate, inertial forces dominate. A Reynolds number based on $U = 1\text{ms}^{-1}$, $l_0 = 0.1\text{m}$ and $\nu = 10^{-6} \text{ m}^2\text{s}^{-1}$ would be $Re_{l_0} = 10^5$, and inertial forces are much larger than viscous forces.

If Reynolds number is based on a length scale y that is decreasing towards 0, Re_y would eventually be $\mathcal{O}(1)$. The viscous forces are then either equal or bigger than the inertial forces.

This close to the wall, the mean velocity depends on the distance y , fluid density ρ , viscosity ν and the wall shear stress τ_w , and is usually called the turbulent boundary layer [12].

By using dimensional analysis, flow behaviour can be expressed by means of dimensionless groups u^+ and y^+ .

The dimensionless groups are given by [12]

$$u^+ = \frac{U}{u_*} \quad (2.12)$$

$$y^+ = \frac{yu_*}{\nu} \quad (2.13)$$

$$u_* = \sqrt{\frac{\tau_w}{\rho}} \quad (2.14)$$

u_* is the friction velocity.

Turbulent boundary layer consists of two regions:

- Inner region, consists of three layers:
 - where viscous stresses dominate,
 - where turbulent stresses dominate,
 - where viscous and turbulent stresses are of similar magnitude.
- outer region
 - inertia dominated flow far from the wall.

The layer where viscous stresses dominate is called the viscous sub-layer. It is a linear relationship between the velocity and distance to the wall and is given as [12]

$$u^+ = y^+ \quad (2.15)$$

The layer is extremely thin, and lies at $y^+ < 5$ [12].

At the layer where turbulent stresses dominate, called the log-layer, the velocity and distance to the wall have a logarithmic relationship. It is given as [12]

$$u^+ = \frac{1}{\kappa} \ln(y^+) + B \quad (2.16)$$

The constants $\kappa = 0.41$ and $B = 5.5$ is found by doing measurements. The log-layer lies outside the viscous sub-layer, at $30 < y^+ < 300$ [12].

Between the viscous sub-layer and the log-layer lies the buffer layer, where the viscous and turbulent stresses are of similar magnitude.

Equations for the viscous sub-layer and log-layer (2.15 and 2.16) are usually called law of the wall and are of great importance in approximating and simulating turbulent boundary layers.

Figure 2.1 is showing a plot containing the viscous sub-layer and the log-layer

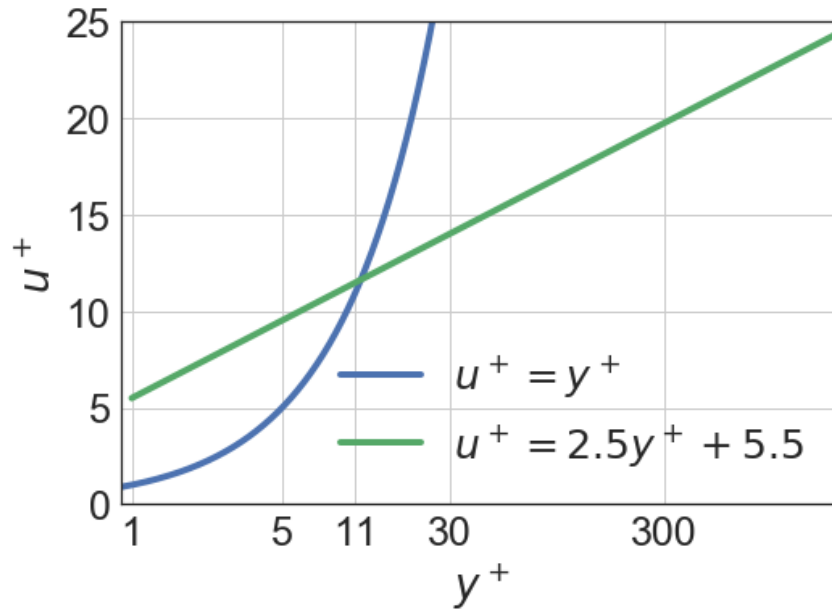


Figure 2.1: Law of the wall

law of the wall; Viscous sub-layer in blue in the range $y^+ < 5$ and log-layer given in green in the range $30 \leq y^+ \leq 300$. Inbetween the viscous sub-layer and log-layer lies the buffer layer. Outer region lies where $y^+ > 300$

2.2.3 Computer modelling of turbulence

The modelling of turbulent fluid flows and the Navier-Stokes equations has seen huge advancements as computer speed increases. The number of applications of fluid flow predictions has grown and computerized analysis has become a crucial part in the field of fluid mechanics.

There are three main methods for numerically solving Navier-Stokes equations:

- Reynolds Averaged Navier Stokes(RANS)
- Large Eddy Simulations(LES)
- Direct Numerical Simulations(DNS)

LES and DNS is introduced rather briefly, while RANS will be introduced in a little bit more detail.

RANS

For many engineering purposes, the focus is on the mean effect of turbulence, and it is unnecessary to resolve the details on all scales.

A key part of RANS is investigating the effects of fluctuations on the mean flow using Reynolds de-composition. The velocity and pressure are decomposed as:

$$\mathbf{u} = \mathbf{U} + \mathbf{u}' \quad (2.17)$$

$$p = P + p', \quad (2.18)$$

where \mathbf{u} is the instantaneous flow field, \mathbf{U} is the mean flow field and \mathbf{u}' is the fluctuating part. The same goes for the pressure, where P is mean and p' is the fluctuating part.

Substituting the de-composed velocity and pressure (2.17, 2.18) into Navier-Stokes equations (2.1, 2.2) and taking the time-mean, the following continuity and momentum equations using suffix notation are derived:

$$\frac{\partial U_i}{\partial x_j} = 0 \quad (2.19)$$

$$\frac{\partial U_i}{\partial t} + \frac{\partial}{\partial x_j}(U_i U_j) = -\frac{1}{\rho} \frac{\partial P}{\partial x_i} + \nu \frac{\partial^2 U_i}{\partial x_j \partial x_j} - \frac{\partial}{\partial x_j}(\overline{u'_i u'_j}). \quad (2.20)$$

Here U_i is the mean velocity, P is the mean pressure and $\overline{u'_i}$ is the mean fluctuating velocity.

In the momentum equation (2.20), the new term $\frac{\partial}{\partial x_j}(\overline{u'_i u'_j})$ is the derivative of the Reynolds stress-tensor [15]. It appears from the convective part $\mathbf{u} \cdot \nabla \mathbf{u}$ of Navier-Stokes equations (2.2), and are not really stresses. The physical meaning of the term is the averaged effect of turbulent advection on the mean flow field [15].

With the new term, the RANS equation is unclosed, with 6 more unknowns appearing from the Reynolds stress-tensor. The four equations have in total 10 unknowns (pressure, three velocity components and six "stresses"). In order to close the problem, enough equations must be found to solve for all the unknowns. In many models, such as one-equation and two-equations models (see [13] chapter 4), the Boussinesq eddy-viscosity approximation [12] is assumed to be valid. The Reynolds stresses are modelled as follows:

$$\tau_{ij} = \overline{u'_i u'_j} = \frac{2}{3} k \delta_{ij} - \nu_t \left(\frac{\partial U_i}{\partial x_j} + \frac{\partial U_j}{\partial x_i} \right) \quad (2.21)$$

$$k = \frac{1}{2} \overline{u'_i u'_i} = \frac{1}{2} (\overline{u_1'^2} + \overline{u_2'^2} + \overline{u_3'^2}) \quad (2.22)$$

where k is the turbulent kinetic energy per unit mass, ν_t is the turbulent or eddy viscosity and δ_{ij} is the Kronecker delta.

Adding the Boussinesq eddy-viscosity approximation (2.21) into the RANS momentum equation (2.20) leads to:

$$\frac{\partial U_i}{\partial t} + \frac{\partial}{\partial x_j}(U_i U_j) = -\frac{1}{\rho} \frac{\partial P'}{\partial x_i} + \frac{\partial}{\partial x_j} \left[(\nu + \nu_t) \frac{\partial U_i}{\partial x_j} \right]. \quad (2.23)$$

where $P' = (P + \frac{2k}{3}\delta_{ij})$, called the modified pressure[14].

To complete the closure of the RANS equations, the eddy viscosity term ν_t needs to be modelled. Dimensional analysis dictates that ν_t needs to be proportional to the product of a characteristic velocity and a characteristic length scale [6, 13]

This paper is using two turbulence models for comparison, namely the two-equation models $k-\epsilon$ and the shear stress transport model $k-\omega$ SST.

$k-\epsilon$ model

The standard $k-\epsilon$ model equations are found in a lot of literature such as [12] and [15].

The $k-\epsilon$ model is perhaps the most widely used, giving good results in classical shear flows. It does however have shortcomings in accurately predicting adverse pressure gradients and boundary layers. Despite its shortcomings, the model is recommended in cases involving multiphase problems by some sources, i.e [6].

The model equations are specified as follows:

Kinematic eddy viscosity equation:

$$\mu_t = \rho C_\mu \frac{k^2}{\epsilon} \quad (2.24)$$

Turbulent kinetic energy equation:

$$\frac{\partial \rho k}{\partial t} + U_j \frac{\partial \rho k}{\partial x_j} = \frac{\partial}{\partial x_j} \left[\frac{(\mu + \mu_t)}{\sigma_k} \frac{\partial k}{\partial x_j} \right] - \rho \epsilon + \rho \tau_{ij} \frac{\partial U_i}{\partial x_j} \quad (2.25)$$

Turbulence dissipation rate equation:

$$\frac{\partial \rho \epsilon}{\partial t} + U_j \frac{\partial \rho \epsilon}{\partial x_j} = \frac{\partial}{\partial x_j} \left[\frac{(\mu + \mu_t)}{\sigma_\epsilon} \frac{\partial \epsilon}{\partial x_j} \right] + \rho C_{\epsilon 1} \frac{\epsilon}{k} \tau_{ij} \frac{\partial U_i}{\partial x_j} - \rho C_{\epsilon 2} \frac{\epsilon^2}{k} \quad (2.26)$$

The model equations use the Boussinesq assumption given in equation (2.21) and contains five adjustable constants: $C_\mu = 0.09$, $\sigma_k = 1.0$, $\sigma_\epsilon = 1.3$, $C_{\epsilon 1} = 1.44$ and $C_{\epsilon 2} = 1.92$

$k-\omega$ SST

$k-\omega$ model is made by Menter [23] and is found in literature and such as [12] and [13].

The $k-\omega$ SST turbulence model is a more advanced model which combines $k-\epsilon$ and $k-\omega$ models. The $k-\epsilon$ model has its shortcomings, as stated above. The $k-\omega$ model was made to better predict adverse pressure gradients and boundary layers, but performed poorer at free streams. Menter [8] proposed a new model which combined the $k-\epsilon$ and the $k-\omega$ models. In literature like [12] it is stated that $k-\omega$ SST model is superior in approximating adverse pressure gradients and boundary layers.

Turbulence resources such as [9] gives thorough description of the model equations. The two-equation model is specified as follows:

Kinematic eddy viscosity equation:

$$\mu_t = \frac{\rho a_1 k}{\max(a_1 \omega, \Omega F_2)} \quad (2.27)$$

Turbulent kinetic energy equation:

$$\frac{\partial \rho k}{\partial t} + U_j \frac{\partial \rho k}{\partial x_j} = \frac{\partial}{\partial x_j} \left[(\mu + \sigma_k \mu_t) \frac{\partial k}{\partial x_j} \right] + \rho P - \beta^* \rho \omega k \quad (2.28)$$

Turbulent specific dissipation rate equation:

$$\frac{\partial \rho \omega}{\partial t} + U_j \frac{\partial \rho \omega}{\partial x_j} = \frac{\partial}{\partial x_j} \left[(\mu + \sigma_{\omega 1} \mu_t) \frac{\partial k}{\partial x_j} \right] + \frac{\gamma}{\nu_t} \rho P - \beta \rho \omega^2 + 2(1 - F_1) \frac{\rho \sigma_{\omega 2}}{\omega} \frac{\partial k}{\partial x_j} \frac{\partial \omega}{\partial x_j} \quad (2.29)$$

Here $P = \tau_{ij} \frac{\partial U_i}{\partial x_j}$, and τ_{ij} is the Boussinesq assumption (2.21). The model constants are given by: $\sigma_k = 0.85$, $\beta^* = 0.09$, $\sigma_{\omega 1} = 0.5$, $\gamma = 0.56$, $\beta = 0.083$ and $\sigma_{\omega 2} = 0.856$.

The additional function F_1 is given by:

$$F_1 = \tanh \left(\arg_1^4 \right) \quad (2.30)$$

and \arg_1 is given by:

$$\arg_1 = \min \left[\max \left(\frac{\sqrt{k}}{\beta^* \omega d}, \frac{500 \nu}{d^2 \omega} \right), \frac{4 \rho \sigma_{\omega 2} k}{CD_{k\omega} d^2} \right] \quad (2.31)$$

$CD_{k\omega}$ is given by:

$$CD_{k\omega} = \max \left(2 \rho \sigma_{\omega 2} \frac{1}{\omega} \frac{\partial k}{\partial x_j} \frac{\partial \omega}{\partial x_j}, 10^{-20} \right) \quad (2.32)$$

Here d is the distance from the field point to the nearest wall and ρ is density.

LES

While RANS have the main focus on the mean flow, LES is resolving large scale turbulence. While the effects of large eddies on the flow are resolved, the effect of the small scale eddies are included by a sub-grid scale models [12].

In LES modeling, a spatial filter is used to separate small scales from large scales. The method is started off with a filtering function and a "cutoff" width, where all scales greater than the "cutoff" width is resolved.

A filtering operation of the filter function is done in the following manner [12]:

$$\bar{\phi}(\mathbf{x}, t) = \int_{-\infty}^{\infty} \int_{-\infty}^{\infty} \int_{-\infty}^{\infty} G(\mathbf{x}, \mathbf{x}' \Delta) \phi(\mathbf{x}', t) dx'_1 dx'_2 dx'_3, \quad (2.33)$$

where $G(\mathbf{x}, \mathbf{x}' \Delta)$ is the filtering function, $\bar{\phi}(\mathbf{x}, t)$ is the filtered function, $\phi(\mathbf{x}', t)$ is the original unfiltered function and Δ is the "cutoff" width. The overbar indicates spatial filtering and not time averaging as with RANS.

Filtering the Navier-stokes equations (2.1 and 2.2) gives the LES continuity and momentum equations as follows:

$$\frac{\partial \bar{u}_i}{\partial x_j} = 0 \quad (2.34)$$

$$\frac{\partial \bar{u}_i}{\partial t} + \frac{\partial \bar{u}_i \bar{u}_j}{\partial x_j} = -\frac{1}{\rho} \frac{\partial \bar{p}}{\partial x_i} + \nu \frac{\partial^2 \bar{u}_i}{\partial x_j \partial x_j} - \frac{\partial \tau_{ij}}{\partial x_j}. \quad (2.35)$$

Here the overline denotes filtered flow variable, and τ_{ij} are the sub-grid scale stresses. The sub-grid scale stresses are part of the unresolved sub-grid scales.

For further introduction of the LES model, Books such as [12] and [11] and papers such as [6] is recommended.

DNS

DNS involves numerical solution of the full Navier-Stokes equations. The method resolves all scales, including the kolmogorov scales (2.9, 2.11 and 2.10). It takes the closed form of the four equations and four unknowns and solves it on a sufficiently fine mesh and small enough time step. For flows with small enough Reynolds number (2.5), DNS can serve as a benchmark for the other turbulence models [6].

Using "Kolmogorov's micro- scales" (2.9 and 2.11), ratio's of the largest and smallest scales can be obtained. The ratio of the largest and the smallest scales are proportional to $Re^{3/4}$ and the ratio of the largest and smallest time scale is proportional to $Re^{1/2}$. $Re = 10^4$ requires a spatial resolution of $\mathcal{O}(10^3)$ in each direction, and the simulation must run for atleast 100 time steps. Computing meshes with 10^9 grid points with 100 time steps is very demanding, even with a modest Reynolds number. Computing industrial flows with higher Reynolds number is impossible with current technology [6, 12].

2.3 Volume of fluid

When there are multiple fluids in a computation, there is need for an interface tracking or interface capturing. To handle multiple-fluid interactions, the volume of fluid-method is used.

For each fluid component, a volume fraction is introduced. If V is a volume of a cell in a computaional domain, and $\alpha(\mathbf{x}, t)$ is the volume fraction, the volume fraction for two fluids are defined as [17]

$$\alpha(\mathbf{x}, t) = \begin{cases} 1, & \mathbf{x} \in \Omega_l \\ 0, & else \end{cases} \quad (2.36)$$

where Ω_l is the part of the domain covered by one fluid l .

On each grid cell, the integral of the color function is approximated. The discrete volume fraction is written as [17]

$$\alpha_i = \frac{1}{V} \int_V \alpha(\mathbf{x}, t) dV \quad (2.37)$$

where the subscript i denotes the i 'th fluid in a system.

For miscible fluids the volume fractions are governed by the advection-diffusion equation given as [16]

$$\frac{\partial \alpha_i}{\partial t} + \nabla \cdot (\alpha \mathbf{u}) = D_{ab} \nabla^2 \alpha, \quad (2.38)$$

Where D_{ab} denotes diffusivity between miscible fluids. The following constraint must be satisfied due to mass conservation:

$$\sum_{i=1}^n \alpha_i = 1 \quad (2.39)$$

Density and viscosity are defined as:

$$\rho = \sum_i \rho_i \alpha_i \quad (2.40)$$

$$\mu = \sum_i \mu_i \alpha_i \quad (2.41)$$

2.4 Numerical discretization

Numerical discretization is the process of transferring differential equations, such as the Navier-Stokes equations (2.1 and 2.2), into discrete counterparts. A discretization method is needed in order to evaluate the equations on computers.

There are three discretisation methods generally used when approximating equations. Finite difference-method, finite element-method and finite volume-method.

As in most commercial well-established CFD codes, this thesis is using the finite volume method. Fvm is one of the most versatile discretization techniques used in cfd [12].

An outline for the discretization procedure can be presented with the following steps:

- Integration of the governing equations of fluid flow all over the finite control volumes of the domain.
- Conversion of the resulting integral equations into a system of algebraic equations.

A steady convection-diffusion equation of a property ϕ without a source term is given as:

$$\nabla \cdot (\rho \mathbf{u} \phi) = \nabla \cdot (\Gamma \nabla \phi), \quad (2.42)$$

where ρ is the density, \mathbf{u} is a known velocity and Γ is diffusivity.

Integrating convection-diffusion equation (2.42) over a control volume (CV) gives:

$$\begin{aligned} \int_{CV} \nabla \cdot (\rho \mathbf{u} \phi) dV &= \int_{CV} \nabla \cdot (\Gamma \nabla \phi) dV \\ \Rightarrow \int_A \mathbf{n} \cdot (\rho \mathbf{u} \phi) dA &= \int_A \mathbf{n} \cdot (\Gamma \nabla \phi) dA. \end{aligned} \quad (2.43)$$

Gauss integration, i.e. Gauss theorem [12] is applied to change the integration over a control volume to an integration over an area.

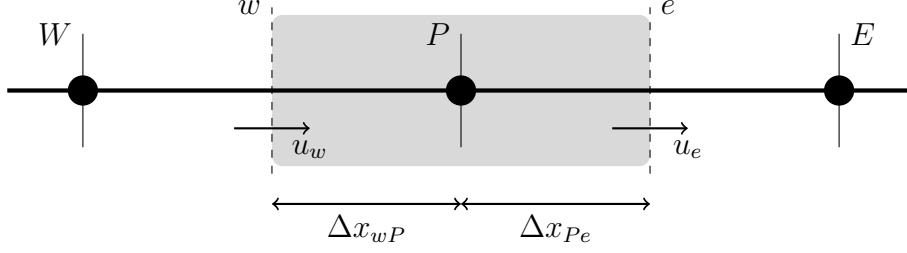


Figure 2.2: Control Volume around a cell center P

In one dimension, and using the control volume shown in figure 2.2, the integration of the convection-diffusion equation (2.43) gives:

$$(\rho u A \phi)_e - (\rho u A \phi)_w = \left(\Gamma A \frac{d\phi}{dx} \right)_e - \left(\Gamma A \frac{d\phi}{dx} \right)_w. \quad (2.44)$$

In order to convert the resulting equation (2.44) into a system of algebraic equations, differencing schemes is used.

Using central differencing on $d\phi/dx$ at the faces e and w and rewriting the property ϕ at the same faces as:

$$\phi_w = \frac{\phi_W + \phi_P}{2} \quad (2.45)$$

$$\phi_e = \frac{\phi_P + \phi_E}{2} \quad (2.46)$$

Substitution of (2.45) and (2.46) into the resulting equation (2.44) yields the central difference expression:

$$\frac{\rho u_e A_e}{2} (\phi_P + \phi_E) - \frac{\rho u_w A_w}{2} (\phi_W + \phi_P) = \Gamma A_e \frac{(\phi_E - \phi_P)}{\Delta x_{PE}} - \Gamma A_w \frac{(\phi_P - \phi_W)}{\Delta x_{WP}} \quad (2.47)$$

Rewriting the central difference expression (2.47), and solving for ϕ_P gives:

$$\left[\left(\frac{\rho u_e}{2} - \frac{\Gamma}{\Delta x_{PE}} \right) A_e - \left(\frac{\rho u_w}{2} - \frac{\Gamma}{\Delta x_{WP}} \right) A_w \right] \phi_P = \left[\left(-\frac{\rho u_e}{2} + \frac{\Gamma}{\Delta x_{PE}} \right) A_e \right] \phi_E + \left[\left(\frac{\rho u_w}{2} + \frac{\Gamma}{\Delta x_{WP}} \right) A_w \right] \phi_W \quad (2.48)$$

With well defined by boundary conditions, the above equation (2.48) can be solved as a system of linear equations i.e.:

$$\mathbf{Ax} = \mathbf{b} \quad (2.49)$$

Where \mathbf{A} is a $m \times n$ matrix, \mathbf{x} is a column vector with n entries and \mathbf{b} is a column vector with m entries.

Using the finite volume-method, the discretizations is carried directly in the physical domain. There is no need for any transformation between the physical and computational coordinate, making the finite volume-method flexible and popular method for computational fluid dynamics [20].

Chapter 3

OpenFOAM

All computational fluid dynamics are structured around numerical algorithms that tackle fluid flow problems. Classical solvers are implemented in well-established CFD codes such as CFX/ANSYS, FLUENT and OpenFOAM. The software used in this thesis is OpenFOAM.

As in all well-established CFD codes, the work flow consists of three main elements:

- pre-processor
- solver
- post-processor

Pre-processing consists of input of a flow problem, in order to make it well-defined before the solving process begins.

The solver is solving the flow problem, by implemented numerical methods and algorithms suitable for the specific problem.

Post-processing consists of verification and validation of the solutions given by the solver. It is essential to investigate data output and visualize. The complexity of fluid flows demands thorough investigation by e.g. comparing with existing experiments, either numerical or experimental.

3.1 Introduction to OpenFoam

This paper is using the free, open source software OpenFOAM (Field Operation and Manipulation). It is a C++ library of source code for solvers and utilities.

Figure 3.1 illustrates an initial state of an OpenFOAM case. Three directories are located in the case folder: 0, constant and system.

The 0 directory contains files for the different variables essential for the problem. Each file defines initial values and boundary conditions for the numerical experiment.

The *constant* directory contains, as the name suggests, all the constants of the case. Constant properties such as gravitation g , density ρ and viscosity ν are put in files *g* and *transportProperties*. Turbulence specifications are set in the file *turbulenceProperties*. The subdirectory *polyMesh* contains the specifics of the mesh geometry.

The *system* directory contains information about meshing of the numerical experiment, how to discretize and solve the equations. The file *controlDict* controls which solver is used, timecontrols and data output controls. As the names suggests, *fvSchemes* and *fvSolution* contains information about discretization schemes and solution algorithms respectively.

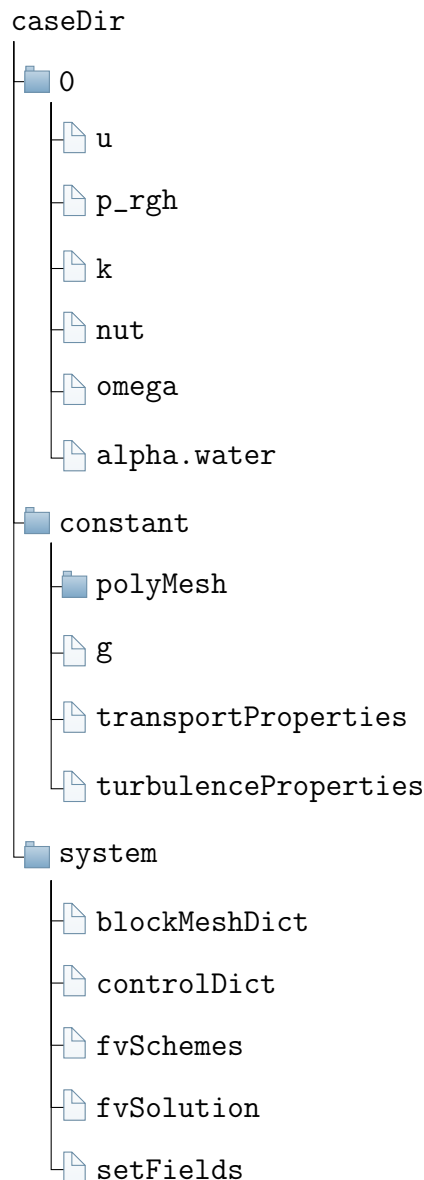


Figure 3.1: Example of case directory structure in openFOAM.

3.2 TwoLiquidMixingFoam

OpenFOAM has solvers for a wide range of applications. As mentioned in the section Introduction to OpenFOAM (3.1), the file *controlDict* found in figure 3.1 defines which solver to use.

Many multiphase solvers can be found, both miscible and immiscible. This thesis is using the incompressible multiphase solver twoLiquidMixingFoam, where the liquids are miscible.

Three equations are being solved. The first equation is the alpha diffusion equation, given by [22]

$$\frac{\partial \alpha_1}{\partial t} + \nabla \cdot (\mathbf{U} \alpha_1) = \nabla \cdot \left(\left(D_{ab} + \frac{\nu_t}{S_c} \right) \nabla \alpha_1 \right) \quad (3.1)$$

where

- α_1 is the volume fraction.
- $\alpha_2 = 1 - \alpha_1$
- $\rho = \alpha_1 \rho_1 + \alpha_2 \rho_2 = \alpha_1 \rho_1 + (1 - \alpha_1) \rho_2$.
- D_{ab} is the molecular diffusivity.
- ν_t is the turbulent eddy viscosity.
- s_c is the turbulent Schmidt number, given as $\mu/(\rho D)$.

The continuity and momentum equation is given, respectively, as:

$$\nabla \cdot \mathbf{U} = 0 \quad (3.2)$$

$$\frac{\partial \rho \mathbf{U}}{\partial t} + \nabla \cdot (\rho \mathbf{U} \mathbf{U}) = -\nabla(p_{rgh}) - gh \nabla \rho + \nabla \cdot (\rho \boldsymbol{\tau}) \quad (3.3)$$

where

- $\boldsymbol{\tau} = -\frac{2}{3} \overline{\mu_{eff}} \nabla \cdot \mathbf{U} \mathbf{I} + \overline{\mu_{eff}} \nabla \mathbf{U} + \overline{\mu_{eff}} (\nabla \mathbf{U})^T$.
- $\overline{\mu_{eff}} = \alpha_1 (\mu_{eff})_1 + \alpha_2 (\mu_{eff})_2$.
- $(\mu_{eff})_i = (\mu - \mu_t)_i$. Subscript i denotes either fluid 1 or 2.

The term $\nabla(p_{rgh})$ and $gh \nabla \rho$ is obtained by using $P = p_{rgh} + \rho gh$. The Solver is using the Boussinesq eddy-viscosity approximation (refeqn:bossinesq), and p is the modified pressure and contains the kinetic energy per unit mass $\frac{2}{3} k \delta_{ij}$.

3.3 Turbulence models

This paper is using the RANS method to estimate turbulence. In order to close the RANS equations, turbulence models are being used. Two different two-equation models are used for comparison of applicability in solving the dead water phenomenon.

The turbulence models used in this project are the $k - \omega$ SST and the $k - \epsilon$ turbulence model. In section Introduction to openFOAM 3.1, the *constant* directory shown in figure 3.1 contains the file *turbulenceProperties*. Here it is defined what simulation type that is being used, i.e. RANS. It also specifies which turbulence model to use.

3.4 Numerical schemes

Having defined the equations to be solved in in section *TwoLiquidMixingFoam* (3.2), the way in which to discretize the equations are defined in the file *fvSchemes* found in figure 3.1. The file consists of sub-dictionaries with name corresponding to terms within the equations given in section *TwoLiquidMixingFoam* (3.2). For each term a numerical scheme must be specified.

Time derivative term $\partial/\partial t$ are discretized by using an *Euler* scheme, a first order implicit difference scheme and is given in the sub-dictionary *ddtSchemes*. The time steps are adjusted during the simulation. That means the time steps used is set during the simulation according to the courant number, given as:

$$C = \frac{u\Delta t}{\Delta x} \quad (3.4)$$

Where u is the velocity. The time steps are adjusted according to a maximum courant number set to 1.0.

The other terms are discretized using finite volume method. As explained in section *Numerical discretization* 2.4, the fvm discretization procedure is done by using gaussian integration and converting the resulting terms into algebraic equations using differencing schemes.

Gradient terms ∇ are set in the sub-dictionary *gradSchemes*. The terms are discretized by using *Gauss linear*, where the *Gauss* entry denotes Gaussian integration and the *linear* entry denotes a central differencing scheme.

Divergence terms $\nabla \cdot$ are set in the sub-dictionary *divSchemes*. There are several divergence terms needing discretization, and specified as:

- *div(rhoPhi,U) Gauss linearUpwind grad(U)*
- *div(phi,alpha) Gauss vanLeer*
- *div(phirb,alpha) Gauss linear*
- *div(phi,k) Gauss upwind*
- *div(phi,omega) Gauss upwind*
- *div(((rho*nuEff)*dev2(T(grad(U)))) Gauss linear*

The *phi* entry in the *div(phi,...)* is the volumetric flux of velocity. *Gauss* entry is the Gaussian integration and last entry is the differencing scheme.

Laplacian terms ∇^2 are set in the sub-dictionary *laplacianSchemes*, and are discretized as *Gauss linear* with the Gaussian integration and a linear differencing scheme.

3.5 Solution algorithms

There are several solution algorithms implemented in openFOAM. Solution procedures are needed in order to obtain solutions to pressure and momentum. In multiphase modelling, additional solution procedures are needed in order to obtain solution to the phase fraction and the volume of fluid method.

There is three different algorithms implemented in OpenFOAM for solving the Navier-Stokes equations (2.2) and (2.1):

- Semi-implicit method for pressure-linked equations SIMPLE algorithm.
- pressure-implicit split-operator PISO algorithm.
- Pressure-implicit method for pressure-linked equations PIMPLE algorithm.

Numerical techniques are required for coupling the pressure and momentum quantities. All algorithms are iterative procedures for coupling momentum and pressure [25]. SIMPLE is a steady state algorithm, PISO is a transient algorithm and PIMPLE is a semi transient algorithm [25].

The twoLiquidMixingFoam solver is using the PIMPLE algorithm for coupling the pressure and momentum. Since it is a multiphase solver, a multi-dimensional limiter for explicit solution i.e MULES algorithm [26] is used for solving the phase fraction α .

Chapter 4

Simulation Design

Whether a numerical experiment is successful depends largely on the pre-processing. A computational domain has to be made well suited to handle the flow problem. Many factors have to be considered in order to have a good numerical experiment, with mesh quality and boundary conditions as the key factors.

4.1 Simulation geometry

The geometry of the numerical experiment is dependent on computational demands. Ideally the geometry of the domain would include the entire barge and a farfield consisting of air, fresh and salt water. A domain including all aspects of the fluid problem would be much more suitable as the case would be more physical.

With a three dimensional problem such as the dead-water phenomenon, the computational costs constrain the experiment to only include some parts of the flow problem. This and the scope of this thesis, which is limited to five months, makes it necessary to make compromise between physics and assumptions. The experiment becomes less physical, but the idea is to isolate certain aspects of the problem to investigate, namely the effects of the internal wave.

The geometry of the computational domain consists of a vessel i.e. the barge draft and a farfield. Farfield includes inlet, outlet, atmosphere, atmosphereFrontOfBarge, bottom, front and back in order to have a closed domain. Since only the draft of the barge is included, the top of the domain located at the free-surface.

Figure 4.1 is showing simulation geometry with name tags of the patches atmosphere, front, inlet and outlet included. The Barge is colored red. The dimensions of the barge is taken from [3] and 0.6 m long (x-dir), 0.45 m wide (y-dir) and 0.35 m wide (z-dir). The geometry has a symmetry plane at the middle of the barge in the y-direction, halving the computational domain. As it only includes what is below the free surface i.e. the draft of the barge, the dimensions of the barge becomes 0.6m long, 0.225m wide. The draft is to 0.1m for all the experiments.

Farfield boundaries are located sufficiently far away to minimize its effects on the solution. International Towing Tank Conference has a practical guidelines for ship CFD applications which states that inlet, outlet and "exterior boundary" should be located

$1 - 2 \times$ length of draft [18]. This experiment is not modelling the free surface as it is a boundary. It does however model an internal wave and in combination with highly unstreamlined draft geometry, the resulting farfield dimensions are:

- inlet located 10.0 m upstream in front of barge.
- outlet located -15.0 m downstream of barge.
- bottom located at -4.0 m below barge.
- back is located 3.0 m at the width side of barge.

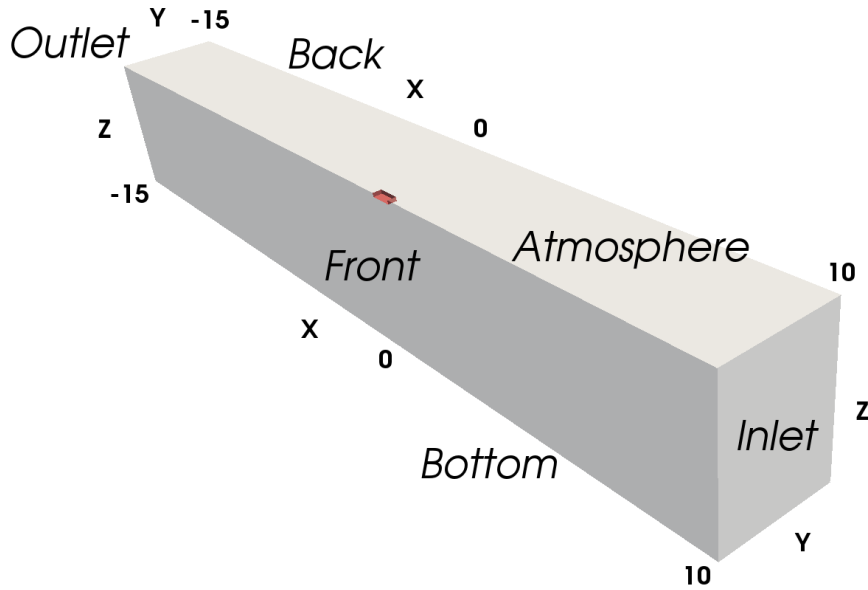


Figure 4.1: Geometry.

Geometry used in the computational experiment. Draft of barge is colored red at $X = 0$ while farfield with patches inlet, outlet, front and atmosphere included.

4.2 Simulation set-up

Simulations are done with a constant draft $D = 0.1$ m. The different experiments are conducted by varying the densimetric Froude number in the range $0.3 \leq Fr_h \leq 1.35$. The densimetric Froude number is varied by changing speeds at constant pycnocline depths giving $h/D = 1, 1.5$ and 2 .

Figure 4.2 is showing a schematic overview of the numerical experiment.

The experiments are done with a moving reference frame, rather than having the barge moving, in order to be able to run simulations sufficiently long and not complicating the mesh too much.

The densities of the fluids are set to 997 kg m^{-3} for fresh water and 1024 kg m^{-3} for salt water. Kinematic viscosity is set to $\nu = 1.79 \cdot 10^{-6} \text{ m}^2 \text{ s}^{-1}$ corresponding to waters at 0°C as done by J. Grue in [5]. Molecular diffusivity and turbulent Schmidt number are

set to respectively $2.0 \cdot 10^{-5}$ and 1.25 as done in the reaserch [22]. The speed varies as $0.08 \leq U \leq 0.22$ corresponding to Reynolds number (2.5) $26815 \leq Re \leq 73743$.

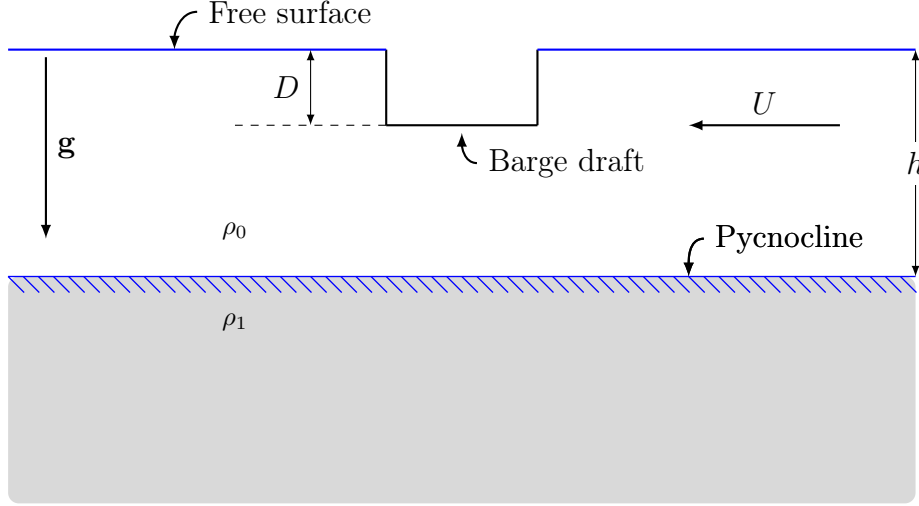


Figure 4.2: Simulation set-up.

Simulations are done by varying speeds U at constant $h/D = 1, 1.5$ and 2 . Densities ρ_0 and ρ_1 are that of fresh and salt water respectively in stratified fluid simulations. For non-stratified fluid simulations, $\rho_0 = \rho_1$.

4.3 Boundary and Initial conditions

Before simulating and solving the numerical experiments, the momentum and continuity equations (2.2 2.1) must have appropriate initial and boundary conditions.

Boundary conditions are required component of the mathematical model that directs the motion of the flow. It specifies the fluxes such as mass and momentum, into and out of the computational domain.

OpenFOAM is representing boundaries as patches consisting of faces, and all inital and and boundary conditions are assigned to the patches. Table 4.1 is showing an overview of all initial and boundary conditions for simulations using the turbulence model k-omega SST .

All descriptions of the boundary conditions are obtain from the source code of OpenFOAM, where usage of the boundary conditions are described. If other wise, it is stated.

Variable Boundary		U	p_rgh	alpha.saltWater	k	omega	nut
Inlet	Type Value	fixedValue internalField	fixedFluxPressure internalField	fixedValue internalField	fixedValue internalField	fixedValue internalField	fixedValue internalField
Outlet	Type Value	O.P.M.V. internalField	zeroGradient -	V.H.F.R. internalField	inletOutlet internalField	inletOutlet internalField	zeroGradient -
Barge	Type Value	M.W.V. (0 0 0)	F.F.P. internalField	zeroGradient -	kqrW.F. internalField	omegaW.F. internalField	nutUSpaldinW.F. internalField
atmosphere	Type Value	slip -	fixedValue internalField	zeroGradient -	zeroGradient -	zeroGradient -	zeroGradient -
atmosphereFrontOfBarge	Type Value	inletOutlet internalField	fixedValue internalField	zeroGradient -	zeroGradient -	zeroGradient -	zeroGradient -
Front	Type Value	symmetryPlane -	symmetryPlane -	symmetryPlane -	symmetryPlane -	symmetryPlane -	symmetryPlane -
Back	Type Value	symmetryPlane -	symmetryPlane -	symmetryPlane -	symmetryPlane -	symmetryPlane -	symmetryPlane -
Bottom	Type Value	symmetryPlane -	symmetryPlane -	symmetryPlane -	symmetryPlane -	symmetryPlane -	symmetryPlane -

Table 4.1: Boundary and initial conditions twoLiquidMixing with k-omega SST turbulence model.

O.P.M.V. = OutletPhaseMeanVelocity, V.H.F.R. = variableHightFlowRate, M.W.V. = movingWallVelocity, F.F.P. = fixedFluxPressure, kqrW.F. = kqrWallFunction, omegaW.F. = omegaWallFunction, nutUSpaldingW.F. = nutUSpaldingWallFunction

4.3.1 U

For velocity U, typical dirichlet boundary condition is applied at the inlet and on the barge. At the inlet it is set a *fixedValue* while a no-slip condition is set at the barge. The no-slip condition is of a special kind, namely *movingWallVelocity*, which is applied for "moving" walls when it is a moving reference frame.

At outlet there is an *outletPhaseMeanVelocity*. This boundary condition adjusts the velocity for the given phase to achieve the specified mean, thus causing the phase-fraction to adjust according to the mass flow rate.

Boundary conditions at the free surface

The free surface waves that is generated when a barge moves at velocities used in these experiments should be of very small wave length and height, due to low Froude numbers (2.6). The Froude number $Fr \leq 0.09$ for all simulations.

Esmailpour et al. [4] conducted a study within the same range of densimetric froude numbers as done in this project. They used a domain containing air, fresh and salt water i.e. the free surface was included. They reported very small waves due to low Froude numbers $Fr \leq 0.05$. For non-stratified flow it was reported that the free surface was flat. For stratified water, the free surface did see a small effect by the internal gravity waves.

Due to the reporting of Esmailpour et al. and computational limitations, the free surface is excluded in this investigation.

Since the simulations only includes what happens below the water surface, and the main focus is on the internal gravity waves, it has been rather tricky to decide boundaries for the free surface.

An approach has been to apply a Neumann boundary condition of zero gradient at the top. With a zero gradient at the top, the bow of the barge would have been well approximated as the fluid hits the bow and it would allow outflow. At the stern however, the lower pressure would allow inflow. This would have been a good approximation, if the inflow had been consisting of air. The problem is that the inflow at the stern would consist of water, causing the interface at the stern to mix and losing of the stratification.

Another approach has been to use a *slip* condition, which is a mix of Dirichlet and Neumann condition. The flow would then be allowed to flow freely in x- and y direction, but be set to zero in z-direction not allowing for in- and outflow. With the low Froude number and the goal of the investigation being the internal wave, this could have been a good approximation. But the *slip* condition caused a numerical artifact at one cell on the bow of the barge with conflicting boundary conditions. This one cell was located where the front and the top intersects on the bow of the barge. The *symmetryPlane* condition at the front of the domain allows for outflow in z-direction. This caused a huge increase of velocity in z-direction at this particular cell.

A compromise has been done, with the top of the domain being split into two patches, namely *atmosphere* and *atmosphereFrontOfBarge*. The *atmosphere* patch having a *slip* boundary condition and the *atmosphereFrontOfBarge* having an *inletOutlet* condition. The *inletOutlet* condition is working as a mix of Dirichlet and Neumann condition, with the specification of inflow, in case there is any.

These boundary conditions have a very engineering approach to them, and is not very physical. But as stated earlier in this report, the main focus is the effect of the internal wave. With the air excluded completely from the simulations, and the low Froude numbers, the final boundary conditions allows for a qualitative reaserch of the dead water phenomenon.

4.3.2 **alpha.saltWater**

The phase fraction *alpha.saltWater* is set in the file *setFieldsDict* where the initial state of the two fluids are set.

For the inlet, Dirichlet condition of a fixed value of either 1 or 0 are set, where 1 is salt water and 0 is fresh water. At the outlet, a *variableHightFlowRate* condition is used. It is a phase fraction condition based upon the flow conditions. Values of *alpha.water* is constrained to lay between specified values of upper and lower bounds of 1 and 0, i.e.

- If *alpha.water* > 1:
 - apply a fixed value, with a uniform level 1.
- If $0 \leq \textit{alpha.saltWater} \leq 1$:
 - apply a *zeroGradient* condition.
- If *alpha.water* < 0:
 - apply a fixed value, with a uniform level 0.

At the *barge*, a Neumann condition of *zeroGradient* is applied. The same goes for *atmosphere* and *atmosphereFrontOfBarge*.

4.3.3 **p_rgh**

For pressure, a *fixedFluxPressure* is used at the *inlet* and on the *barge*. The pressure is not known at *inlet*. The *fixedFluxPressure* is a Neumann condition that is accounting for the flux specified by the velocity set at the boundary.

Since the velocity is set to 0 by the *noSlip* boundary condition on the *barge*, the Neumann condition becomes a *zeroGradient* in reality.

At the *athmospere* and *atmosphereFrontOfBarge* patches there is Dirichlet boundary of *fixedValue* 0. At the outlet there is a Neumann boundary condition of *zeroGradient*.

4.3.4 Turbulence properties k, nut, omega and epsilon

All of the turbulence properties nut, k, omega and epsilon are set with a Neumann condition of *zeroGradient* at *atmosphere* and *atmosphereFrontOfBarge*.

At the inlet, Dirichlet boundaries are set as a fixed value, calculated from equations for setting farfield turbulence conditions.

Farfield turbulent kinetic energy is set as recommended in [19] by using:

$$k = \frac{3}{2}(UI)^2, \quad (4.1)$$

where U is the freestream speed and I is the turbulence intensity, usually set below 1% for cases similar to this experiment.

Farfield omega conditions is set by using [27]

$$\omega = \frac{\sqrt{k}}{C_\mu^{1/4} l_t} \quad (4.2)$$

where $C_\mu = 0.09$ and l_t is the turbulent length scale, set to $l/100$ where l is the length of the barge.

Turbulent dissipation rate epsilon is set as recommended in [19] by using:

$$\epsilon = \frac{c_\mu^{3/4} k^{3/2}}{l_t} \quad (4.3)$$

The turbulent viscosity for $k - \omega$ SST is set by using:

$$\nu_t = \frac{k}{\omega} \quad (4.4)$$

Finally, the turbulent viscosity for $k - \epsilon$ is set by using:

$$\nu_t = C_\mu \frac{k^2}{\epsilon} \quad (4.5)$$

Wall functions

Wall functions are used to avoid resolving all scales in the boundary layer. The wall functions use the dimensional analysis of the boundary layer and law of the wall presented in section 2.2.2 to estimate values near the wall.

Wall functions are applied as boundary conditions for all the turbulence properties at the barge.

Turbulent viscosity *nut* is using the wall function *nutUSpaldingWallFunction*. The function is using a special curve fit of the law of the wall, in order to be applicable in the whole boundary layer [21].

For turbulent kinetic energy k , the wall function *kqrWallFunction* has been used. It uses the log-law layer (2.16) to estimate values for the boundary. Using this wallFunction would require a distance of the first cell adjacent to the barge to be $y^+ > 30$.

This has not been fulfilled with the meshes used in this report, but brief test runs with a wall function applicable for smaller values of y^+ , has been conducted after the mistake was discovered. *kLowReWallFunction* did not make any signifacant effects on the calculated drag in these test runs. A comparison of the wall functions with pycnocline depth $h/D = 1.5$ and $Fr_h = 0.69$ showed that *kqrWallFunction* had a difference of 0.007% in calculated drag compared to *kLowReWallFunction*

For *omega* and *epsilon*, the wall functions *omegaWallFunction* and *epsilonWallFunction* has been used. Both wall functions are applicable for a wide range of y^+ values.

4.4 Mesh and mesh convergence

The outcome of a numerical experiment is highly dependent on the mesh quality. A multiphase simulation investigating drag and internal waves needs a mesh suitable to capture the phenomenon. At the same time the mesh has to account for computational cost, as the computational resources available is rather limited for the scope of this thesis.

4.4.1 Meshing procedure

The base mesh is made by defining a *blockMeshDict* file that generates a mesh as the one shown in figure 4.3. The base mesh is made to be uniform in the spatial x- and y-direction, except for z-direction, where it is refined to better capture the pycnocline in the entire computational domain. Number of cells in the base mesh is 12668. In order to increase mesh quality, refinement is needed.

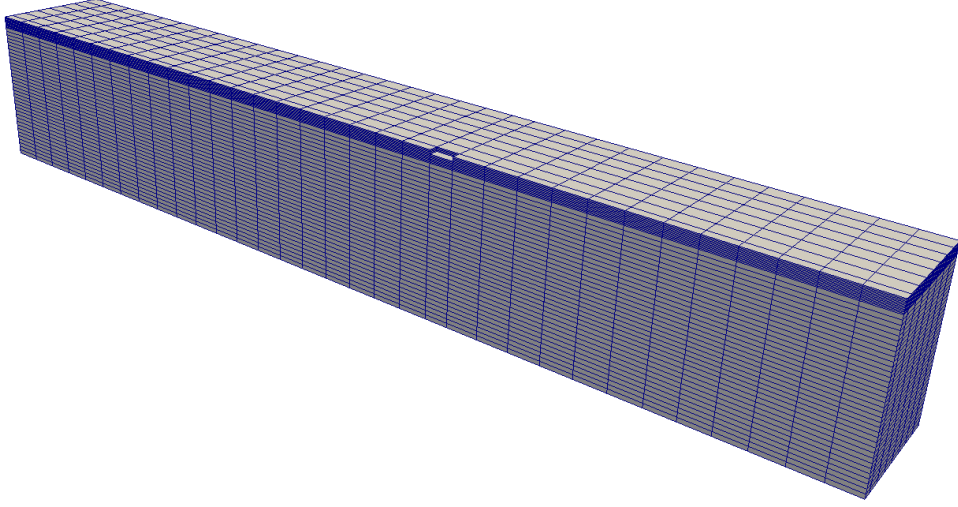


Figure 4.3: Base mesh generated by blockMesh

The base mesh made in blockMeshDict and generated by blockMesh consists of 12668 cells. It has uniform spatially distribution in x- and y- direction, while z-direction is refined in the area where pycnocline is located.

To refine the mesh further, *topoSetDict* and *refineMeshDict* files has been used. In a *topoSetDict*, an area within the mesh is defined in which it is desirable to refine the mesh. The *refineMeshDict* refines the mesh in the specified area in the desired direction. *RefineMeshDict* refines the mesh by splitting every cell in two within the specified area and in the specified direction.

By using *topoSetDict* and *refineMeshDict* it is easy to refine the mesh in the important areas within the domain i.e. boundary layer and below the barge at the pycnocline. It is further a useful tool in the means of maintaining cell aspect ratios, which is the ratio of the longest to the shortest side of the cell. Cell aspect ratio can have significant effect on waves in openFOAM [24]. The areas of the domain which almost is un-disturbed can be left out from refining, making the mesh less computational demanding.

Figure 4.4 is showing the mesh after refinemenmt which consists of 744794 cells.

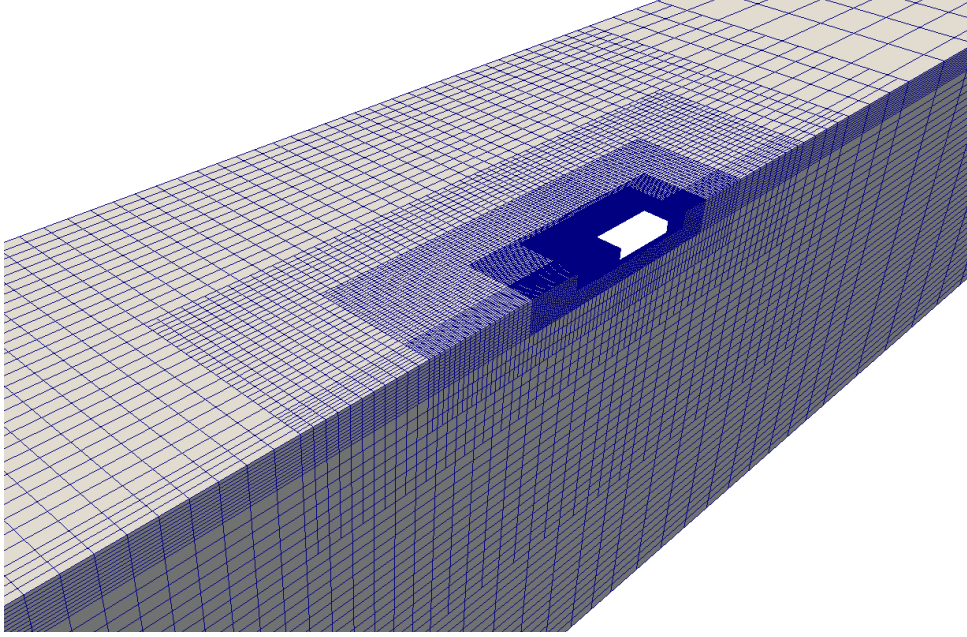


Figure 4.4: Mesh after refinement

The mesh after beeing refined consists of 744794 cells. Max aspect ratio = 32.7

4.4.2 Convergence tests

Three mesh grids have been systematically refined to evaluate grid convergence. It is done by using a grid refinement ratio of 2 on the base mesh. The resulting course, medium and fine grids have 4.2×10^5 , 7.4×10^5 and 1.3×10^6 cells respectively. The reason for not having a refinement ratio of 2 on the resulting grids is that the same *topoSetDict* and *refineMeshDict* files are used. The resulting grids do not necessarily get the same refinement ratio, as the refinement procedure using *topoSetDict* and *refineMeshDict* depends on the base mesh.

Two speeds at two different pycnocline depths are used to check for convergence, resulting in four tests. For each pycnocline depth, two velocities give densimetric Froude number corresponding to near-peak drag coefficient and densimetric Froude number close to super critical.

Figure 4.5 and 4.6 are showing test runs with pycnocline located at 0.1m ($h/D = 1$) below the barge and with $Fr_h = 0.86$ and $Fr_h = 1.35$ respectively. Turbulence model used in the tests are the $k - \omega$ SST. The tests show that there is not much difference between the medium and fine grids, while the coarse grid is oscillating.

Table 4.2 shows the average y^+ values obtained from the convergence tests. The y^+ values lie all within the buffer layer. The y^+ values increase when simulations are conducted with higher velocity. The idea is to make the mesh and have wall-functions applicable for all the range of y^+ values in the experiments.

Mesh \ Fr_h	0.86	1.35
Coarse	11.14	13.10
Medium	8.39	11.33
Fine	6.8	8.95

Table 4.2: Average y^+ values for pycnocline at 0.1m

Average y^+ value obtained from running convergence tests.

All y^+ values lies within the buffer layer, with the finest mesh tending towards viscous sub-layer

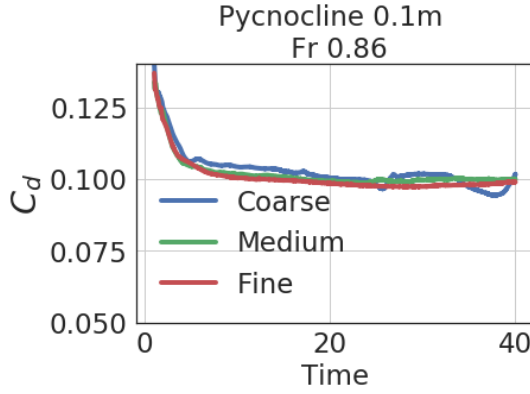


Figure 4.5: C_d as a function of time. Grid convergence test run with three different grids; coarse, medium and fine. Pycnocline located at 0.2 m below the barge, and $Fr_h = 0.61$. The medium and fine grids are converging towards the same drag coefficient, while the coarse grid is oscillating around the medium and fine grids

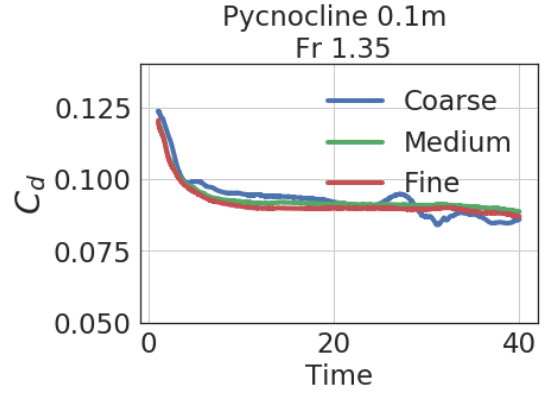


Figure 4.6: C_d as a function of time. Grid convergence test run with three different grids; coarse, medium and fine. Pycnocline located at 0.2 m below the barge, and $Fr_h = 0.61$. The medium and fine grids are converging towards the same drag coefficient, while the coarse grid is oscillating around the medium and fine grids

Figure 4.7 and 4.8 are showing test runs with pycnocline located at 0.2m ($h/D = 2$) below the barge with $Fr_h = 0.61$ and $Fr_h = 0.95$ respectively. This test is also conducted with the turbulence model $k - \omega$ SST. The tests show the same trends as the tests done with pycnocline located 0.1m below the barge.

Table 4.3 shows the average y^+ values obtained from the convergence tests with pycnocline located at 0.2m below the barge. The y^+ values lies all within the buffer layer.

$\backslash Fr_h$	0.61	0.95
Mesh		
Coarse	11.89	14.50
Medium	9.74	11.53
Fine	7.73	9.51

Table 4.3: Average y^+ values for pycnocline at 0.2m

Average Y^+ value obtained from running convergence tests.

All Y^+ values lies within the buffer layer, with the finest mesh tending towards viscous sub-layer

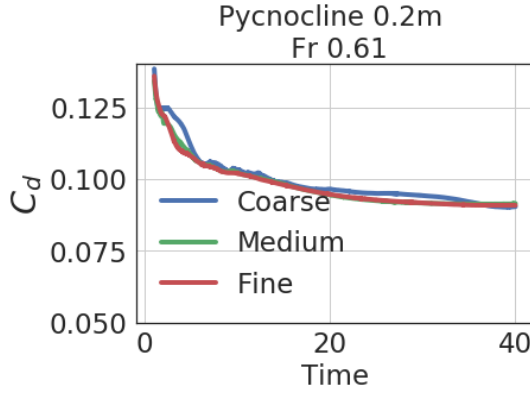


Figure 4.7: C_d as a function of time. Grid convergence test run with three different grids; coarse, medium and fine. Pycnocline located at 0.2 m below the barge, and $Fr_h = 0.61$. The medium and fine grids are converging towards the same drag coefficient, while the coarse grid is oscillating around the medium and fine grids

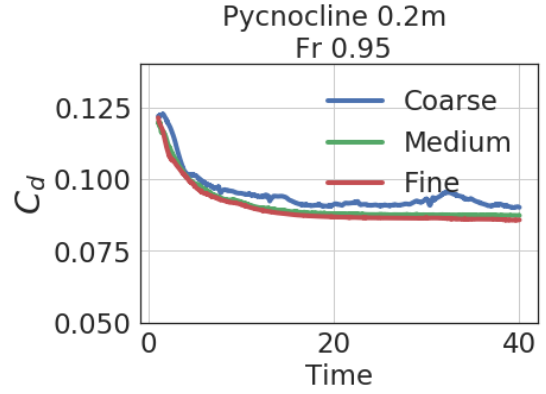


Figure 4.8: C_d as a function of time. Grid convergence test run with three different grids; coarse, medium and fine. Pycnocline located at 0.2 m below the barge, and $Fr_h = 0.61$. The medium and fine grids are converging towards the same drag coefficient, while the coarse grid is oscillating around the medium and fine grids

From the convergence tests it is clear that it is not much to gain convergence wise by using a finer mesh. The resulting C_d 's are very similar comparing the medium and fine grids. By using the medium mesh, computational time is saved and many more simulations can be done within the time frame of this thesis.

Chapter 5

Results

5.1 Comparison of turbulence models

Comparison of the turbulence models were done by running numerical experiments with the exact same mesh. Pycnocline depth was set to 0.2m below the barge. Two cases are presented, the first with a densimetric Froude number $Fr_h = 0.69$ and the second with $Fr_h = 0.95$. The first test lies within the range where Fr_h should give peak C_d and the second test where Fr_h should give a lower C_d that tend towards a non-stratified fluid case.

The comparison is done by checking convergence of C_d for the two cases. The motivation for comparing the C_d and not any other parameters is that of the main scope of this project, investigating the increase in C_d in sub critical densimetric Froude number experiments. It is essential to have a turbulence model that best approximate the C_d

The first test is shown in figure 5.1. From the figure it is shown that the turbulence model $k - \omega$ SST gives a good convergence of the C_d . The model $k - \epsilon$ on the other hand sees a rise in C_d throughout the entire experiment and get even more unstable as time increases.

The second test is shown in figure 5.2, and the same trend is seen as in the first test. $k - \omega$ SST gives a good convergence, while $k - \epsilon$ get a rise in C_d as time increases. In the second test, $k - \epsilon$ even starts to oscillate as the time increases.

From the tests it is concluded that $k - \omega$ SST model is the most reliable in terms of investigating the "dead water" phenomenon going further.

Even though the theory states that the $k - \omega$ turbulence model yields better results when simulating adverse pressure gradients and boundary layer [12], it serves a purpose to compare with other models. As stated in theory, the $k - \epsilon$ model can get reliable results when simulating multiphase fluids. The comparison of the models only confirms the theory that the $k - \omega$ SST model is superior in estimating boundary layers and adverse pressure gradients.

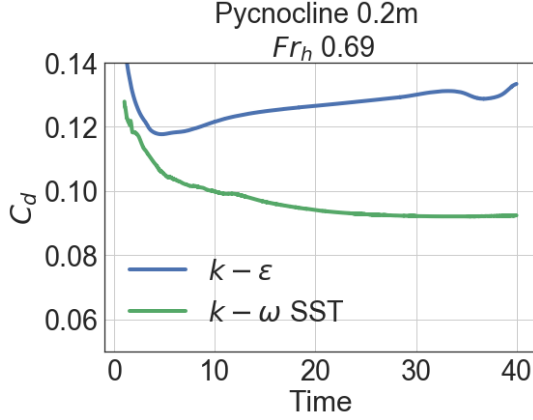


Figure 5.1: C_d as a function of time. Simulations done with a pycnocline at 0.2m and $Fr_h = 0.69$. $k - \epsilon$ Turbulence model yields a higher C_d than the $k - \omega$ SST model. While the $k - \omega$ SST model converges, $k - \epsilon$ model has a steady increase of C_d and gets more unstable as time passes

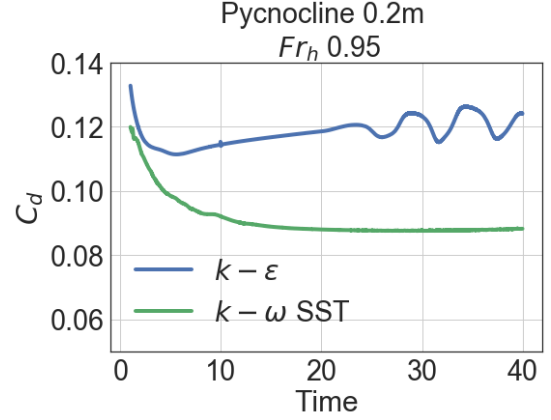


Figure 5.2: C_d as a function of time. Simulations done with a pycnocline at 0.2m and $Fr_h = 0.95$. $k - \epsilon$ Turbulence model yields a higher C_d than the $k - \omega$ SST model. While the $k - \omega$ SST model converges, $k - \epsilon$ model has a steady increase of C_d and starts to oscillate as time passes

5.2 Drag

5.2.1 Non-stratified fluid

Non-stratified fluid simulations were conducted by simulating with a density corresponding to fresh water, and with barge draft $D = 0.1\text{m}$ at speeds $0.06\text{ms}^{-1} \leq U \leq 0.24\text{ms}^{-1}$.

Gou et.al conducted the same experiment in a towing tank [3], with a barge that has the same dimensions as used in this thesis. Their results showed that drag force is directly proportional to the square of the towing speed, which means that the C_d is constant.

Results of the non-stratified fluid simulations are shown along with the results obtained by Gou et.al. [3] in figure 5.3. This thesis is getting similar results to the results reported by Gou et al. as both experiments obtained a linear curve.

The current study underpredicts the drag force obtained by Gou et.al. by $\approx 20\%$. There may be several reasons for the under-prediction of drag. Reason one being that the Gou et.al study did experiments in a shallow and narrow water tank, while this simulation domain is much larger. Another reason is the approach of not including what is above water line and excluding the free surface.

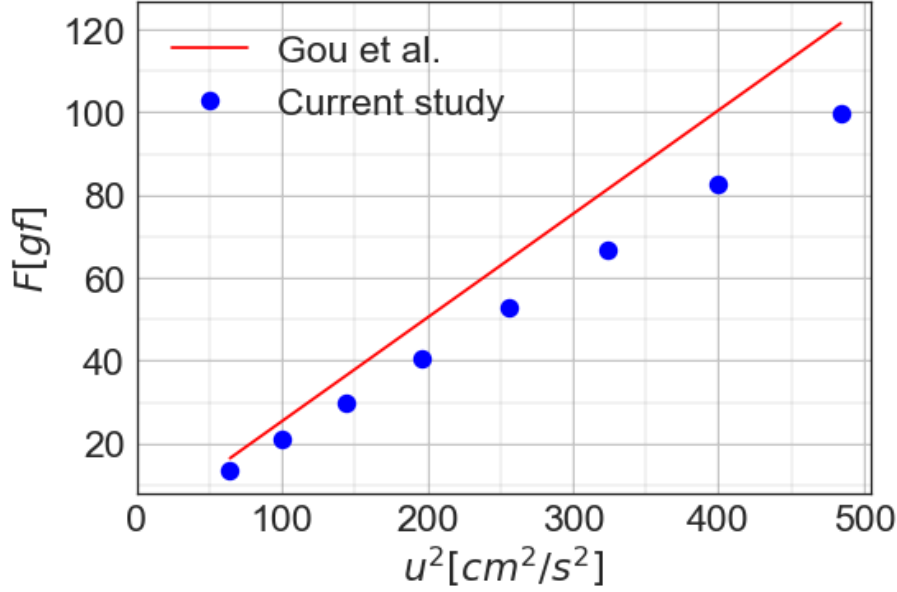


Figure 5.3: Drag force as function of velocity squared.

Drag force in non-stratified fluid with draft = 0.1. Simulations is in good agreement with experimental data obtained on an identical barge done by Gou et. al. [3] with a deviance of $\approx 20\%$. Drag force is directly proportional to the square of the towing speed, which means that the C_d is constant.

5.2.2 Stratified fluids

Study of the behaviour of resistance in a stratified fluid is conducted by simulating with barge draft $D = 0.1$ and pycnocline depths $h/D = 1, 1.5$ and 2 . All three set ups are then simulated with speeds corresponding to densimetric Froude numbers (2.7) in the range of $0.35 \leq Fr_h \leq 1.35$

The drag coefficients shown in figure 5.4 offers a lot of information. A clear pattern of increasing C_d are shown for all three pycnocline depths. All C_d peaks are found within the range of $0.6 \leq Fr_h \leq 0.7$, with pycnocline depth $h/D = 1$ giving the largest C_d . All three set-ups have the same pattern of increasing C_d until Fr_h reaches peak region, then decreasing and tending towards non-stratified fluid flow.

Similar trends are presented in the study done by Esmailpour et. al. [4] who are doing computational fluid dynamics study on a ship moving in stratified water. Esmailpour et. al. reported peaks in a higher region than obtained in the thesis, with densimetric Froude numbers between $Fr_h = 0.83$ and $Fr_h = 0.91$.

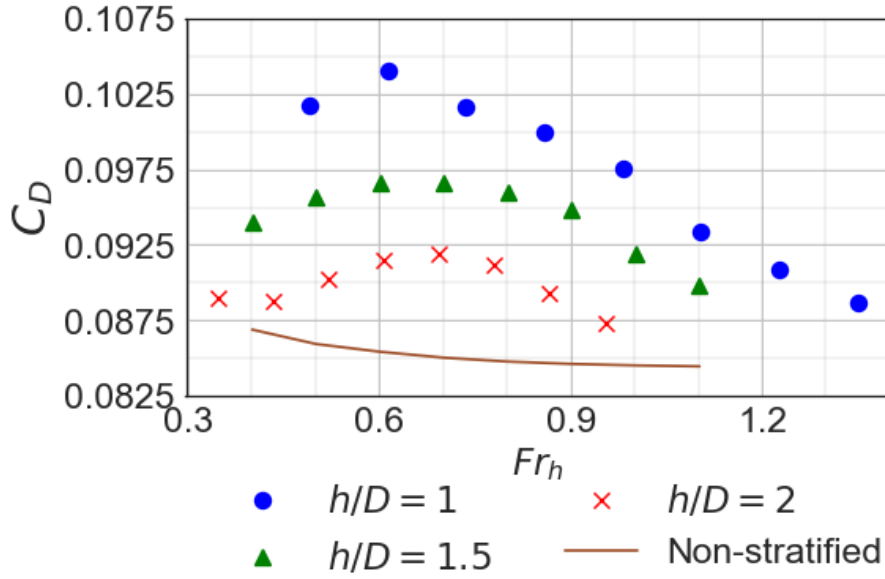


Figure 5.4: Drag coefficient as function of Fr_h

Drag coefficients (C_d) obtained by running simulations with pycnocline depth $h/D = 1$, 1.5 and 2. C_d peaks within a range of $Fr_h = 0.6$ and 0.8 . C_d tends towards simulations of non-stratified fluid for all pycnocline locations when $Fr_h \leq 0.6$ and $Fr_h \geq 0.8$.

Esmailpour et.al. is also reporting a much more significant increase in C_d than is obtained in this thesis. The peak C_d for a pycnocline depth of $h/D = 1$ has an increase of 600%.

Percentage increase of C_d in a stratified fluid compared to a non-stratified fluid is presented in figure 5.5. Pycnocline depth $h/D = 1$ have a percentage increase of 21%, much smaller than Esmailpour. Pycnocline depth $h/D = 1.5$ have an increase of 13.5%, while Esmailpour et.al has an increase of 450% with the same pycnocline depth.

Looking into the large difference in the increase of C_d , the question arises of the exclusion of the free-surface. The effects of the free-surface might be too significant in stratified waters to leave out the free surface. Another key difference in the approach done by Esmailpour et.al. is the number of grids. The study was conducted with a grid consisting of 21.9×10^6 cells, to properly resolve boundary layer and internal wave appearing at the pycnocline.

Despite of the small amount of increase in C_d obtained from the simulations, the effect of the stratified fluid is clearly apparent. The increase in drag appears in the same manner presented in Gou et.al. [3]. It is also in accordance with the findings in the study of FRAM's dead water resistance conducted by Grue [5]. Grue

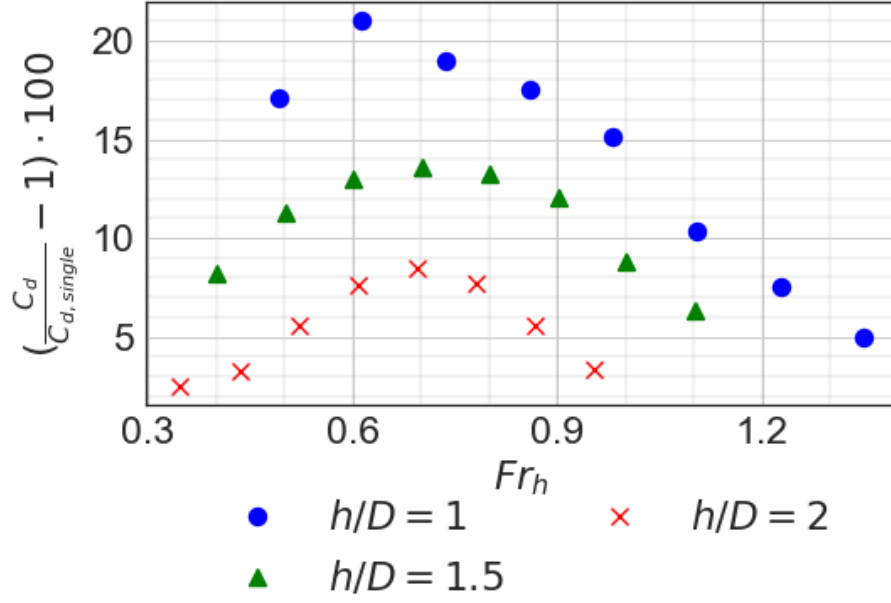


Figure 5.5: Percentage difference as function Fr_h .

Percentage difference between stratified and non-stratified fluid. Pycnocline depth of $h/D = 2$ gives a peak increase of 8.5%. $h/D = 1.5$ gives peak increase of 13.5% and $h/D = 1$ gives peak increase of 21%

5.3 Internal wave and its effect

Any kind of vessel or boat moving in stratified fluid experience increase in drag compared to non-stratified fluid. As the barge propagates in the stratified fluid, internal gravity waves appear below and in the wake of the barge. The numerical experiments is clearly catching this phenomenon.

Figure 5.6 is a visualization of the internal gravity waves below the barge. It is showing a contour of the interface tracking volume fraction *alpha.saltWater* for a pycnocline depth $h/D = 2$, and velocity located at the symmetry plane. The figure is showing a clear wave pattern below and in the wake, and is a useful tool for visualizing the phenomenon to gain qualitative understanding.

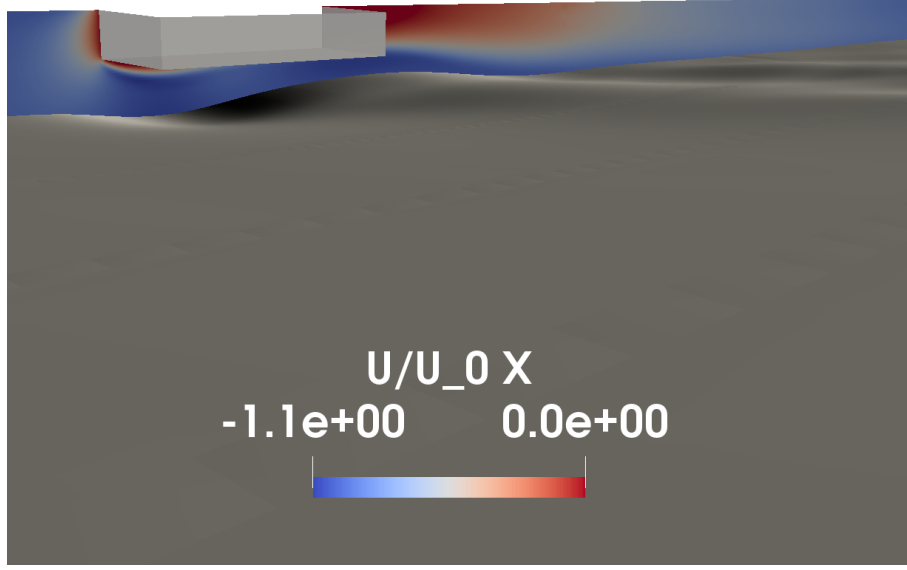


Figure 5.6: Velocity and internal gravity wave.
Contour of the value fraction α with pycnocline depth $h/D = 2$. An internal gravity wave appears below the barge. The non dimensional velocity U_x/U_{0x} is shown in the symmetryplane of the domain.

5.3.1 Internal waves and effect on velocity

The densimetric Froude number (2.7) is a ratio of the velocity of the barge and the celerity of the longest internal waves. As Fr_h increase, the largest crest of the internal waves are going to be located at further back towards the stern of the barge, and eventually in the wake.

Figure 5.7 is showing the location of the pycnocline as a function of it position below the barge. The three cases shown in the figure corresponds to Fr_h where C_d starts to increase, Fr_h at peak C_d and Fr_h where C_d has decreased and almost reached a C_d obtained by non-stratified simulations.

The location of the internal waves corresponding to peak C_d are located in the wake and almost right below the stern of the barge. The internal waves are causing restriction of passage area, and the flow is accelerated. Acceleration of the fluid flow is thinning the boundary layer and causing a drop in pressure.

Figure 5.8, is showing non-dimensional velocity profiles scaled by the far field velocity. The velocity profile corresponding to the internal wave located below the stern of the barge shows increase in velocity as it approaches the stern. This in turn makes the pressure drop and a thinning of the boundary layer, causing an increase in C_d .

Pycnocline depth $h/D = 1.5$ is telling the same story as for pycnocline depth $h/D = 2$. Looking at figure 5.9 and figure 5.10, the internal wave located below the stern of the barge corresponding to peak C_d is causing the increase in velocity.

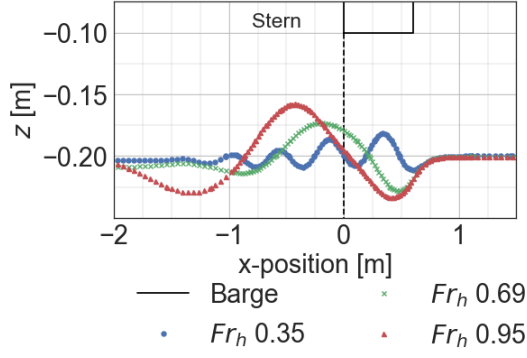


Figure 5.7: Pycnocline as a function of x-position.

Initial pycnocline depth $h/D = 2$. As Fr_h increases, wave amplitude increase and the crest located further back. Location of crest has significant effect on flow field as shown in figure 5.8. The internal wave restricts the passage area, causing a significant increase in speed.

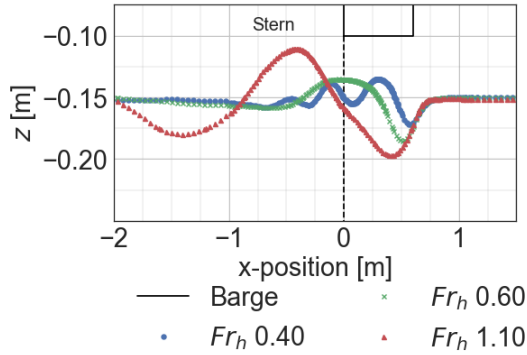


Figure 5.9: Pycnocline as a function of x-position.

Initial pycnocline depth $h/D = 2$. As Fr_h increases, wave amplitude increase and the crest located further back. Location of crest has significant effect on flow field as shown in figure 5.10. The internal wave restricts the passage area, causing a significant increase in speed.

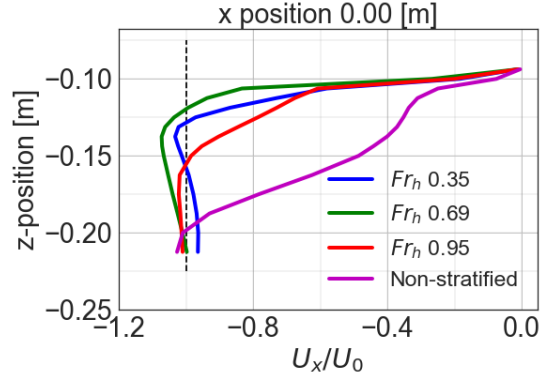


Figure 5.8: velocity profiles U_x/U_0 as function of z-position.

Dimensionless velocity profiles U_x/U_0 below barge at $x = 0.0m$ with pycnocline at $0.2m$. The velocity profile with $Fr_h = 0.69$ has a significant increase in speed and greater gradient, resulting in the peak drag coefficient.

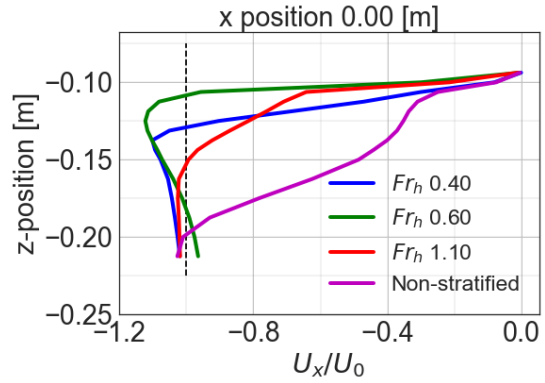


Figure 5.10: velocity profiles U_x/U_0 as function of z-position.

Dimensionless velocity profiles U_x/U_0 below barge at $x = 0.0m$ with pycnocline at $0.2m$. The velocity profile with $Fr_h = 0.69$ has a significant increase in speed and greater gradient, resulting in the peak drag coefficient.

Looking at velocity profiles midships at $x = 0.30\text{m}$ in fig 5.12 and 5.12, it is clearly an acceleration of the flow caused by the wave also located midships. Since the wave is located midships, it is not effecting C_d as much as the one located at the stern. A pressure drop midship below the barge is not as significant as one located at the stern.

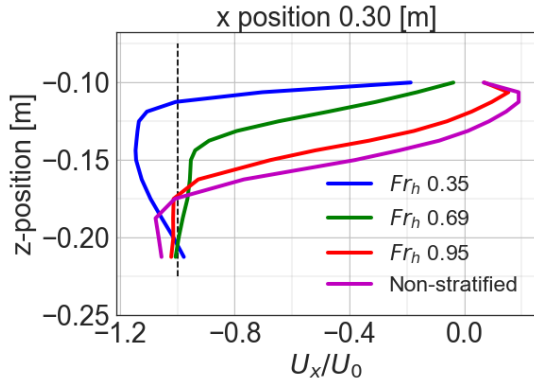


Figure 5.11: velocity profiles U_x/U_0 as function of z-position.

Dimensionless velocity profiles U_x/U_0 below barge at $x = 0.3\text{m}$ with pycnocline at 0.2m . The velocity profile with $Fr_h = 0.35$ has a significant increase in speed and greater gradient, as the amplitude of the internal wave is located near the same location.

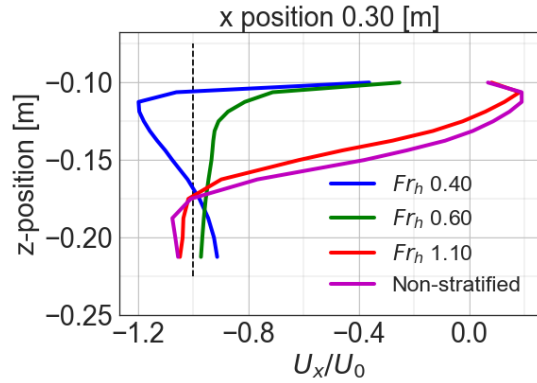


Figure 5.12: velocity profiles U_x/U_0 as function of z-position.

Dimensionless velocity profiles U_x/U_0 below barge at $x = 0.3\text{m}$ with pycnocline at 0.15m . The velocity profile with $Fr_h = 0.40$ has a significant increase in speed and greater gradient, as the amplitude of the internal wave is located near the same location.

Chapter 6

Conclusions and further recommendations

6.1 Conclusions

Computational fluid dynamics have been used to investigate drag resistance on a barge in stratified and non-stratified waters. The free open source software OpenFOAM has been used to get a qualitative understanding of the dead water phenomenon.

A comparison of the RANS turbulence models $k - \epsilon$ and $k - \omega$ SST has been conducted to determine which model is most applicable for the investigation. The comparison consists of convergence tests of the drag coefficients C_d on the barge with draft $D = 0.1\text{m}$ and a pycnocline depth $h/D = 2$. $k - \omega$ SST model was suspected to give the best results, which was shown. The $k - \omega$ SST model converged and gave stable results. The $k - \epsilon$ model was found to be unstable, not converging and even oscillating for simulations with densimetric Froude number $Fr_h = 0.95$.

Simulations of a non-stratified fluid showed similar behaviour as obtained by Gou et al. [3]. The non stratified fluid simulations were shown to have a constant C_d , and to have a drag force directly proportional to the square of the simulation speed. Simulations yielded results with a deviance of $\approx 20\%$ compared to results from Gou et al.

Simulations of stratified fluid mostly agree with results obtained by Gou et al [3], J. Grue [5] and Esmailpour [4]. Increase in C_d is shown in all simulations with densimetric Froude number in regions of $0.35 \leq Fr_h \leq 0.6$. Peak C_d was found in regions $0.6 \leq Fr_h \leq 0.7$ and decrease for $Fr_h > 0.7$ with C_d tending towards non-stratified simulations as Fr_h increased. The same trend was shown for all pycnocline depths $h/D = 1, 1.5$ and 2 . Gou et al. reported peak in regions $0.5 \leq Fr_h \leq 0.6$, while Esmailour et al. reported peaks in regions $0.83 \leq Fr_h \leq 0.93$.

The increase in drag of stratified fluid was found to be much smaller than reported by Gou et al. and Esmailpour et al., with a maximum increase of 21% in C_d compared to a non-stratified fluid. Esmailpour reported a maximum increase in C_d of 600% . Even though their study was conducted on a completely different vessel, their reported increase is suggesting under-estimation in this report. The reason for the under-estimation of C_d may be the exclusion of the free surface. It is also likely to be due to insufficient number

of grid points. Esmaeilpour had around 20 times more grid points compared to this study, with around 20 million cells.

The internal gravity waves and their location below the barge were found to have significant effect on the flow field. The speed is accelerated by the restriction of passage area by the internal wave. The waves corresponding to the peak C_d caused a significant increase in the velocity at the stern, causing a drop of pressure.

6.2 Further recommendations

Further recommendations regarding investigations on the dead water phenomenon, a lot of improvements and approaches can be advised.

As this project only focused on the internal wave, and leaving out the free surface waves, it would be of great interest to include the free surface waves in the investigation. A better resolved mesh is advised, especially around the pycnocline. Simulations with pycnocline depths $h/D \leq 1$ should be studied to see for which pycnocline depth a maximum resistance is obtained, and for which depth the effect decreases again.

Comparison of other turbulence models e.g. Spalart-Allmaras model is advised, as it is said to have good performance for flows with adverse pressure gradients and boundary layers [12]. A study of sensitivity to numerical discretization schemes may be conducted, in order to obtain higher order of accuracy and stability. Also conducting a comparison of large eddy simulations with RANS simulations is of interest.

Experiments in a towing tank, allowing for measuring of resistance in combinations with tools to investigate velocity profiles such as particle image velocimetry (PIV) should be conducted. A combination of both experiments and CFD could lead to an even better qualitative understanding of the phenomenon.

Bibliography

- [1] F. Nansen
Farthest North, Westminster: Archibald Constable and Company
2 Whitehall Gardens, 1897. Vol 1.
- [2] V.W. Ekman
On dead-water in The Norwegian North Polar Expedition 1893-1896. Scientific Results.
Edited by F. Nansen (Brogger, christiania, 1904)
- [3] Y. Guo, W. Xu, X. Xinwei, and B. Teng,
Experiment study on the towing resistance of a barge in a two-layer fluid.
In The 32nd International Workshop on Water Waves and Floating Bodies, 2017.
- [4] Mehdi Esmaeilpour, J. Ezequiel Martin, Pablo M. Carrica
Computational Fluid Dynamics Study of the Dead Water Problem
Journal of Fluids Engineering, October, 2017.
- [5] John Grue
calculating FRAM's dead water
Springer Verlag, 2018
- [6] C.D. Argyropoulos, N.C. Markatos, (2015). Recent advances on the numerical
modelling of turbulent flows, Applied Mathematical Modelling
<https://www.sciencedirect.com/science/article/pii/S0307904X14003448#bi0005>
- [7] F.M. White, Viscous Fluid Flow
(second ed.), McGraw Hill, New York (1991)
- [8] F. R. Menter
Review of the shear-stress transport turbulence model experience from an industrial
perspective,
International Journal of Computational Fluid Dynamics (2009)
https://www.tandfonline.com/doi/full/10.1080/10618560902773387?scroll=top&needAccess=true#_i3
- [9] Turbulence Modeling Resource
<https://turbmodels.larc.nasa.gov/sst.html>
- [10] Frans T.M. Nieuwstadt, Bendiks J. Boersma, Jerry Westerweel, Turbulence, Intro-
duction to Theory and Applications of Turbulent Flows
Springer, Delft (2015)

- [11] L. C. Berselli T. Iliescu W. J. Layton
Mathematics of Large Eddy Simulation of Turbulent Flows
Springer, Pisa, Blacksburch and Pittsburgh (2005)
- [12] H. K. Versteeg, W. Malalasekera, An introduction to Computational Fluid Dynamics,
The Finite Volume method
(second edition) , Pearson, Loughborough (2007)
- [13] D. Wilcox
Turbulence Modelling for CFD
(third ed.), DCW Industries, Inc (2006)
- [14] S. P. Pope.
Turbulent Flows.
Cambridge University Press, 2000.
- [15] P. Durbin, B. A. Petterson Reif
Statistical Theory and Modeling for Turbulent Flows
(second ed.), Wiley & Sons, West Sussex (2011)
- [16] By Kai Bao, Xiaolong Wu, Hui Zhang and Enhua Wu
Volume fraction based miscible and immiscible fluid animation
Comp. Anim. Virtual Worlds (2010) <http://citeseerx.ist.psu.edu/viewdoc/download?doi=10.1.1.459.7375&rep=rep1&type=pdf>
- [17] Gregor Černe, Stojan Petelin † and Iztok Tiselj
Coupling of the Interface Tracking and the Two-Fluid Models for the Simulation of Incompressible Two-Phase Flow
Journal of Computational Physics 171, 776–804 (2001) https://ac.els-cdn.com/S002199910196810X/1-s2.0-S002199910196810X-main.pdf?_tid=30dd869d-b73f-4eed-ab23-6157367259eb&acdnat=1523609023_364c3bac9fcaf02d04d3586a5b9a78c4
- [18] International Towing Tank Conference,
Recommended Procedures and Guidelines, Practical Guidelines for Ship CFD Applications <https://ittc.info/media/1357/75-03-02-03.pdf>
- [19] Volker Bertram,
Practical Ship Hydrodynamics
Butterworth-Heinemann, Oxford (2000)
- [20] Fadl Moukalled, Marwan Darwish, and Luca Mangani.
The Finite Volume Method in Computational Fluid Dynamics An Advanced Introduction with Open-FOAM(R) and Matlab
volume 113 of Fluid Mechanics and its applications. Springer-Verlag, 2015.
- [21] D. B. Spalding,
A Single Formula for the "Law of the Wall",
Journal of Applied Mechanics, (1961).

- [22] Rok Krpan and Boštjan Končar
Simulation of Turbulent Wake at Mixing of Two Confined Horizontal Flows Science and Technology of Nuclear Installations, Volume 2018 "Jožef Stefan" Institute, Ljubljana, Slovenia <https://www.hindawi.com/journals/stni/2018/5240361/>
- [23] Menter, F. R.
Two-Equation Eddy-Viscosity Turbulence Models for Engineering Applications
AIAA Journal, Vol. 32, No. 8, August 1994, pp. 1598-1605.
- [24] Johan Roenby, Bjarke Eltard Larsen, Henrik Bredmose and Hrvoje Jasak
A new volume of fluid method in OpenFOAM
VII International Conference on Computational Methods in Marine Engineering, MARINE 2017
- [25] OpenFOAM user guide version 5.0
<http://foam.sourceforge.net/docs/Guides-a4/OpenFOAMUserGuide-A4.pdf>
- [26] OpenFOAM 2.3.0: Multiphase Modelling MULES
<https://openfoam.org/release/2-3-0/multiphase/>
- [27] Turbulence free stream conditions https://www.cfd-online.com/Wiki/Turbulence_free-stream_boundary_conditions